Mon. Not. R. Astron. Soc. **000**, 1–?? (2015) Printed 30 September 2015 (MN LATEX style file v2.2)

Sh2-138: Physical environment around a small cluster of massive stars

T. Baug,[1⋆] D.K. Ojha,[1] L.K. Dewangan,[2] J.P. Ninan,[1] B.C. Bhatt,[3] S.K. Ghosh [1,4] and K.K. Mallick[1]†

[1] *Tata Institute of Fundamental Research, Homi Bhabha Road, Colaba, Mumbai 400005, India*
[2] *Instituto Nacional de Astrofísica, Óptica y Electrónica, Luis Enrique Erro # 1, Tonantzintla, Puebla, México C.P. 72840, México*
[3] *Indian Institute of Astrophysics, Koramangala, Bangalore 560 034, India*
[4] *National Centre for Radio Astrophysics, Tata Institute of Fundamental Research, Pune 411 007, India*

arXiv:1509.08716v1 [astro-ph.SR] 29 Sep 2015

Submitted

ABSTRACT

We present a multi-wavelength study of the Sh2-138, a Galactic compact H II region. The data comprise of optical and near-infrared (NIR) photometric and spectroscopic observations from the 2-m Himalayan *Chandra* Telescope, radio observations from the Giant Metrewave Radio Telescope (GMRT), and archival data covering radio through NIR wavelengths. A total of 10 Class I and 54 Class II young stellar objects (YSOs) are identified in a 4.′6×4.′6 area of the Sh2-138 region. Five compact ionized clumps, with four lacking of any optical or NIR counterparts, are identified using the 1280 MHz radio map, and correspond to sources with spectral type earlier than B0.5. Free-free emission spectral energy distribution fitting of the central compact H II region yields an electron density of ∼2250±400 cm^{-3}. With the aid of a wide range of spectra, from 0.5-15 μm, the central brightest source - previously hypothesised to be the main ionizing source - is characterized as a Herbig Be type star. At large scale (15′ ×15′), the *Herschel* images (70–500 μm) and the nearest neighbour analysis of YSOs suggest the formation of an isolated cluster at the junction of filaments. Furthermore, using a greybody fit to the dust spectrum, the cluster is found to be associated with the highest column density (∼3×10^{22} cm^{-2}) and high temperature (∼35 K) regime, as well as with the radio continuum emission. The mass of the central clump seen in the column density map is estimated to be ∼3770 $M_{\odot}$.

Key words: stars: formation - stars: luminosity function - ISM: individual objects: Sh2-138 - infrared: ISM - H II regions - radio continuum: ISM

1 INTRODUCTION

Massive stars (> 8 M$_{\odot}$) influence the evolution of their host galaxies in a multitude of ways, through stellar winds, outflows, expanding H II regions, and supernova explosions (Zinnecker & Yorke 2007). They are also the primary source of heavy elements, and their ultraviolet (UV) radiation can inject vast amounts of energy and momentum into the natal medium. However, the formation and interaction of massive stars with their surrounding environment is not yet well understood, though it is well-accepted that they are usually associated with clusters (Duchêne & Kraus 2013). This empirical property of massive stars requires thorough observational studies of young stellar clusters in the Galaxy. More recently, with the advent of far-infrared (FIR) and submillimetre (sub-mm) observations, such clusters have been often found to be associated with filamentary structures (André et al. 2010; Schneider et al. 2012). However, a study of such young stellar clusters, along with the role of filaments in the formation and evolution of dense massive star-forming clumps, is currently a matter of active investigation.

Sh2-138 (Sharpless 1959) is a Galactic compact H II region (α_{2000} ∼ 22$^{\rm h}$32$^{\rm m}$46$^{\rm s}$, δ_{2000} ∼ +58$^{\rm d}$28$^{\rm m}$22$^{\rm s}$), associated with IRAS 22308+5812 (also referred as $IRAS$ source in this work). It harbors a stellar cluster which is dominated by at least four O–B2 stars (Deharveng et al. 1999), with a total luminosity of ∼4.9×10^4 L$_{\odot}$ (Simpson & Rubin 1990). Deharveng et al. (1999) studied the optical spectra of the brightest object present in the stellar cluster and suggested that this source could be a Herbig Ae/Be candidate. Radio continuum emission at 4.89 GHz (beam ∼13″), with a diameter of ∼1.′5 (∼2.5 pc at a distance of 5.7 kpc), was detected near the $IRAS$ source by Fich (1993). A study of the densest parts of this region, as well as the molecular boundaries, was carried out by Johansson et al. (1994) using the isotopomers of CO, CS, SO, CN, HCN, HNC, HCO$^+$ and H$_2$CO. Qin et al. (2008) reported bipolar molecular outflows towards the $IRAS$ source with an entrainment

⋆ E-mail: tapas.baug@tifr.res.in (TB)
† This file has been amended to highlight the proper use of LATEX 2$_{\varepsilon}$ code with the class file.

rate of $\sim$22.5 $\times$ $10^{-4} M_{\odot}$ yr^{-1} using the CO $J = 3 - 2$ and $J = 2 - 1$ line emissions. Electron density calculation, based on the fine structure lines of [Ar II–III], [S III], and [Ne II] from the Infrared Space Observatory (ISO) spectra, suggests that the Sh2-138 is a classical H II region (Martín-Hernández et al. 2002).

Deharveng et al. (1999) use a distance estimate of 5 kpc for the Sh2-138 region, assuming it to be a part of the same complex as the nearby regions with similar velocities. They basically use the mean distance of these other nearby regions, whose individual distances have large variation, from 3.45-5.9 kpc. However, the kinematic distance calculation by Deharveng et al. (1999), based on the CO ($J = 1 - 0$) observations of Blitz, Fich & Stark (1982), yields a distance of 5.9$\pm$1.0 kpc. A similar distance of $\sim$5.7 kpc is calculated by Wouterloot & Brand (1989) using radial velocity data from their ^{12}CO ($J = 1 - 0$) observations. Hence, we adopt a value of 5.7$\pm$1.0 kpc for our work.

The previous studies on the Sh2-138 region using optical and near-infrared (NIR) observations have demonstrated the presence of ongoing star formation in a stellar cluster containing at least four massive stars. However, those studies were mainly focused within an area of $\sim 2' \times 2'$ encompassing the stellar cluster. An overall morphological study of the region, and its relation to the ongoing star formation and stellar population, is still pending. Additionally, the study of physical environment of the Sh2-138 region at a large scale is yet to be explored observationally. Furthermore, the advent of FIR and sub-mm observatories like *Herschel* has provided opportunity to explore the large-scale structures, as well as investigate theories such as the role of filaments in the formation of stellar clusters (Myers 2009; Schneider et al. 2012; Mallick et al. 2013, 2015). Since star formation in a region is a sum of many components, it is helpful to carry out an overall study at various wavelengths. In this work, we have performed a detailed multi-wavelength analysis of the Sh2-138 region from 25 pc to 0.1 pc scale centered on IRAS 22308+5812. This has been done using new optical and NIR photometric and spectroscopic observations, as well as radio observations, from Indian observational facilities, complemented with the multi-wavelength data covering radio through NIR wavelengths from publicly available surveys.

In Section 2, we present the observations of the Sh2-138 region and data reduction techniques. Other available archival data sets used in this paper are summarized in Section 3. Morphology of the region inferred using multi-wavelength observations is presented in Section 4. In Section 5, we discuss the nature of the brightest star detected in the region using optical, NIR, and mid-infrared (MIR) spectra. The identification and selection of young stellar objects (YSOs) are presented in Section 6, followed by a general discussion in Section 7, and a presentation of the main conclusions in Section 8.

2 OBSERVATIONS AND DATA REDUCTIONS

2.1 Optical $BVRI$-band Photometry

Optical $BVRI$ imaging observations of the Sh2-138 region were carried out on 2005 September 8 using the Himalaya Faint Object Spectrograph and Camera (HFOSC) mounted on the 2 m Himalayan $Chandra$ Telescope (HCT). HFOSC is equipped with a SITe 2k$\times$4k pixels CCD and the central 2k$\times$2k pixels of the CCD are used for imaging. With a plate scale of $\sim$0.3 arcsec pixel^{-1}, it covers a field of view of $\sim 10' \times 10'$ on the sky. Images were obtained with long and short exposures in the Bessell B (600s, 60s, 20s), V (600s, 20s, 5s), R (300s, 20s, 5s), and I (200s, 10s, 3s) band filters. Bias and twilight flat frames were also observed in each filter. The $BVRI$ images of the standard field SA 114-176 (Landolt 1992) were obtained for photometric calibration as well as for the extinction coefficients estimation. Observations were performed with an average seeing of 1.″5 full width at half maximum (FWHM).

Basic processing of the CCD frames was done using the IRAF[1] data reduction package. The astrometric calibration of these frames was performed using the Two Micron All Sky Survey (2MASS; Skrutskie et al. 2006) coordinates of 12 point sources (spread throughout the frame), and a positional accuracy better than $\pm 0.''08$ was obtained. Due to the crowded nature of the Sh2-138 region, point spread function (PSF) photometry was carried out using the IRAF DAOPHOT package (Stetson 1987). The PSF was generated from several isolated stars (> 9) present in the frame. Magnitudes estimated from both short and long exposure frames, for each filter, were averaged to obtain the instrumental magnitudes. However, we have used magnitudes obtained in the short exposure frames for bright sources which are saturated in the long exposure frames. Instrumental magnitudes of broad-band images were converted to the standard values using the colour correction equations available for the HFOSC. The 10σ limiting magnitudes were found to be 21.3, 22.4, 21.8 and 20.6 for the B-, V-, R-, and I-bands, respectively. In $\sim 10' \times 10'$ FoV centred on $IRAS$ source, we found a total of 685, 1979, 2573 and 2582 sources upto the 10σ detection limit in B-, V-, R-, and I-bands, respectively.

2.2 Optical Spectroscopy

2.2.1 Slitless $H\alpha$ Spectroscopy

In order to identify strong $H\alpha$ emission sources in the Sh2-138 region, slitless $H\alpha$ spectra were obtained using the HFOSC on 2007 November 16. The spectra were observed using a combination of grism 5 (5200-10300 Å) and wide-$H\alpha$ filter (6300-6740 Å), with a spectral resolution of 870. The central 2k$\times$2k part of the 2k$\times$4k CCD was utilized for observations. Three slitless spectra, with an exposure time of 420s each, were obtained for the region and were finally coadded to increase the signal-to-noise ratio. Image frames without grism were also observed to positionally match the stars with their slitless spectra. These observations directly allow us to trace the stars with enhanced $H\alpha$ emission with respect to the continuum.

2.2.2 Slit Spectroscopy

Optical spectroscopic observations of the central brightest source were performed using the HFOSC on 2014 November 18. The slit ($1.''92 \times 11'$) spectrum was obtained using grism 8 (5800-8350 Å; R$\sim$2190), for an exposure time of 40 min. Several bias frames and FeNe calibration lamp spectrum were also obtained for bias subtraction and wavelength calibration, respectively, of the observed spectrum. A spectroscopic standard (HIP 14431) was observed for telluric corrections. The observed spectrum was reduced using the IRAF data reduction package.

[1] Image Reduction and Analysis Facility (IRAF) is distributed by the National Optical Astronomy Observatory, USA

2.3 NIR JHK_s-band photometry

The newly installed TIFR Near Infrared Spectrometer and Imager Camera (TIRSPEC) on the HCT was used for NIR observations on 2014 November 18 under photometric conditions with an average seeing of 1.″4. TIRSPEC is equipped with a 1024×1024 pixels HAWAII-1 PACE array which, with a pixel scale of about 0.″3, translates to a field of view $\sim$5′×5′. The details of the instrument can be found in Ninan et al. (2014). We performed deep photometric observations of the Sh2-138 region in J (1.25 μm), H (1.65 μm), and K_s (2.16 μm) bands. Multiple frames, with a single frame's exposure time being 20s, were acquired at 7 dithered positions. After rejecting bad frames, we obtained 57, 54, and 56 good frames which provide an effective on-source integration time of 1140s, 1080s, and 1120s in J-, H-, and K_s-bands, respectively. Flat field and sky frames were also observed for flat correction and sky subtraction of the object frames. The astrometric calibration was done using 2MASS coordinates of 30 point sources present in the frames. The positional accuracy was found to be better than ±0.″15.

A semi-automated script written in PyRAF (Ninan et al. 2014) was used for reduction of the observed images following the standard procedure. Due to crowded field of the region, PSF photometry was performed on NIR images using the 'ALLSTAR' algorithm of the DAOPHOT package. Isolated bright stars (>9) were used to determine the PSF. The instrumental magnitudes were further corrected using the colour correction equations for TIRSPEC (given in Ninan et al. 2014). The resultant magnitudes were calibrated to 2MASS system using about 15 isolated stars having error <0.04 mag. Our final catalog is comprised of sources in an area of 4.′6×4.′6 after removing stars at the edges of the observed frames. The 10σ limiting magnitudes were found to be 18.2, 18.0, and 17.8 for the J-, H-, and K_s-bands, respectively. We found a total of 617, 674, and 703 sources upto the 10σ detection limit in J-, H-, and K_s-bands, respectively.

We have evaluated the completeness limit of TIRSPEC K_s-band image using artificial star experiments. Artificial stars with different magnitudes were added in the image, and then it was determined what fraction of these added stars were detected, per 0.5 magnitude bin, using DAOFIND task in IRAF. Finally, it was found that the recovery rate was more than 90% for the sources with $K_s \leqslant$14.5 mag.

2.4 NIR spectroscopy

We obtained NIR spectra of the central brightest source on 2014 May 29, using the TIRSPEC, in NIR Y (1.02-1.20 μm), J (1.21-1.48 μm), H (1.49-1.78 μm), and K (2.04-2.35 μm) bands. Average spectral resolution of TIRSPEC is $\sim$1200. We obtained a total of 8 spectra at two dithered positions in each band, with an exposure time of 100s for each spectrum, which gives on-source integration time of 800s in each band. Corresponding NIR continuum and Argon lamp spectra were obtained for continuum subtraction and wavelength calibration, respectively, of the observed spectra. Spectra of a separate spectroscopic standard star (HIP 14431) were also observed for telluric correction. All the spectra were reduced using a semi-automated script written in PyRAF (Ninan et al. 2014). The spectra were extracted using the APALL task in IRAF. Finally, all the JHK-band spectra were flux calibrated using the magnitudes derived from the TIRSPEC photometry. Y-band spectrum was calibrated using the flux determined at 1.05 μm by interpolating I- and J-band fluxes.

Table 1. Log of Optical and NIR observations

Filter	Exposure Time (sec) × No. of frames	Date of Obs.	Instrument/FoV
	Imaging		
B	600×1, 60×1, 20×1	2005 Sep 08	HFOSC/10′×10′
V	600×1, 20×1, 5×1	2005 Sep 08	HFOSC/10′×10′
R	300×1, 20×1, 5×1	2005 Sep 08	HFOSC/10′×10′
I	200×1, 10×1, 3×1	2005 Sep 08	HFOSC/10′×10′
$H\alpha$	600×1, 250×1, 50×1	2005 Sep 08	HFOSC/10′×10′
J	20×57	2014 Nov 18	TIRSPEC/5′×5′
H	20×54	2014 Nov 18	TIRSPEC/5′×5′
K_s	20×56	2014 Nov 18	TIRSPEC/5′×5′
Methane off	30×17	2014 Jun 06	TIRSPEC/5′×5′
$[Fe\ II]$	30×15	2014 Jun 06	TIRSPEC/5′×5′
H_2	30×15	2014 Jun 06	TIRSPEC/5′×5′
$Br\gamma$	30×15	2014 Jun 06	TIRSPEC/5′×5′
K-cont	30×15	2014 Jun 06	TIRSPEC/5′×5′
	Spectroscopy		
Slitless-$H\alpha$	420×3	2007 Nov 16	HFOSC/10′×10′
Slit-optical	2400×1	2014 Nov 18	HFOSC/–
Slit-NIR-Y	100×8	2014 May 29	TIRSPEC/–
Slit-NIR-J	100×8	2014 May 29	TIRSPEC/–
Slit-NIR-H	100×8	2014 May 29	TIRSPEC/–
Slit-NIR-K	100×8	2014 May 29	TIRSPEC/–

2.5 Optical and NIR narrow-band imaging

We conducted optical narrow-band imaging observations of the region in $H\alpha$ filter (λ $\sim$6563 Å, $\Delta\lambda$ $\sim$100 Å) with exposure times of 600s, 250s, and 50s on 2005 September 8 using the HFOSC. There was no separate narrow-band continuum image observed, and hence, the optical R-band image was used for continuum subtraction.

NIR narrow-band observations were also obtained in $[Fe\ II]$ (1.645 μm; Bandwidth: 1.6%), H_2 (2.122 μm; Bandwidth: 2.0%), and $Br\ \gamma$ (2.166 μm; Bandwidth: 0.98%) filters on 2014 June 6 using TIRSPEC mounted on the HCT. Observations were also carried out in Methane off band (1.584 μm; Bandwidth: 3.6%) for continuum subtraction of $[Fe\ II]$ images, and in K-continuum band (2.273 μm; Bandwidth: 1.73%) for continuum subtraction of H_2 and $Br\gamma$ images. To obtain continuum-subtracted images, each set of narrow band frames was aligned and transformed to same PSF using IRAF tasks. The final continuum subtracted H_2 and $[Fe\ II]$ images were binned in 6×6 pixels to enhance the signal-to-ratio of the images.

The log of all optical and NIR observations is given in Table 1.

2.6 Radio Continuum Observations

Radio continuum observations of the Sh2-138 region at 610 and 1280 MHz bands were carried out using the Giant Metrewave Radio Telescope (GMRT) on 2002 May 19 (Project Code 01SKG01) and 2002 September 27 (Project Code 02SKG01), respectively. The GMRT consists of 30 antennas and each antenna is 45m in diameter. For an approximate 'Y'-shaped configuration, 12 antennas of

the GMRT are randomly distributed in the central 1x1 km^2 region, and remaining 18 are placed along three arms (arm length upto ∼14 km). The maximum baseline of GMRT is about 25 km. Primary beam size is about 43 arcmin and 26 arcmin for 610 and 1280 MHz, respectively. More details on the GMRT array can be found in Swarup et al. (1991).

Total observations time at 610 and 1280 MHz bands was 2.2 hours and 3.6 hours, respectively. The data reduction was carried out using the Astronomical Image Processing Software (AIPS) package, following similar procedure as described in Mallick et al. (2013). The data were edited to flag out the bad baselines or bad time ranges using the AIPS tasks. Multiple iterations of flagging and calibration were done to improve the data quality, which was finally Fourier-inverted to make the radio maps. A few iterations of (phase) self-calibration were carried out to remove the ionospheric phase distortion effects. The final 610 and 1280 MHz images have a synthesised beamsize of $5\farcs5\times4\farcs8$ and $3\farcs4\times2\farcs3$, respectively.

Our source is located towards the Galactic plane while the corresponding flux calibrator (3C48) is situated away from the Galactic plane. At meter wavelengths, a large amount of radiation comes from the Galactic plane which increases the effective antennae temperature. Hence, it was important to correct both 610 and 1280 MHz images for system temperature (see Omar, Chengalur & Roshi 2002; Mallick et al. 2012; Vig et al. 2014). It was done by rescaling both the images by a correction factor of (T_{freq} + T_{sys})/T_{sys}, where T_{sys} is the system temperature obtained from GMRT Web site, and T_{freq} is the sky temperature at the observed frequency (i.e., 610 and 1280 MHz) towards the source obtained using the interpolated value from the sky temperature map of Haslam et al. (1982) at 408 MHz.

3 ARCHIVAL DATA

We have also obtained publicly available multi-wavelength archival data to investigate the ongoing physical processes in the Sh2-138 region.

3.1 UKIDSS *JHK* data

United Kingdom Infrared Deep Sky Survey (UKIDSS) archival data of the Galactic Plane Survey (GPS release 6.0; Lawrence et al. 2007) are available for the Sh2-138 region. UKIDSS observations were obtained using the UKIRT Wide Field Camera (WFCAM; Casali et al. 1998). UKIDSS J-band magnitudes are not available for many sources in the central $2'\times2'$ nebular region. Therefore, we retrieved the UKIDSS sources detected in all the three NIR (JHK) bands as well as detected only in the H- and K-bands. Note that UKIDSS (with 3.8 m telescope) data allow us to identify much redder sources than TIRSPEC (with 2 m telescope) in H- and K_s-bands. For example, sources are detected upto $H-K\ \sim\ 1.6$ using TIRSPEC, while the reddest source detected in UKIDSS in the same field of view (FoV) has $H-K\ \sim\ 3.1$. We selected only reliable photometry following the conditions given in Lucas et al. (2008). The TIRSPEC and UKIDSS catalogs were cross-matched in the central $4\farcm6\times4\farcm6$ area with a matching radius of $1''$. The redder UKIDSS sources, which are not detected in TIRSPEC, were combined with TIRSPEC catalog to make the final NIR catalog for the $4\farcm6\times4\farcm6$ area centered on IRAS 22308+5812. A comparison between TIRSPEC and UKIDSS photometry was performed by plotting the differences of UKIDSS and TIRSPEC magnitudes with respect to TIRSPEC magnitudes (shown in Figure 1). We obtained differences of 0.00±0.22, -0.07±0.19, and 0.00±0.24 mag in J-, H- and K_s-bands, respectively. Note that there could be variable sources which are possibly causing scatter in the difference between magnitudes obtained at two epochs.

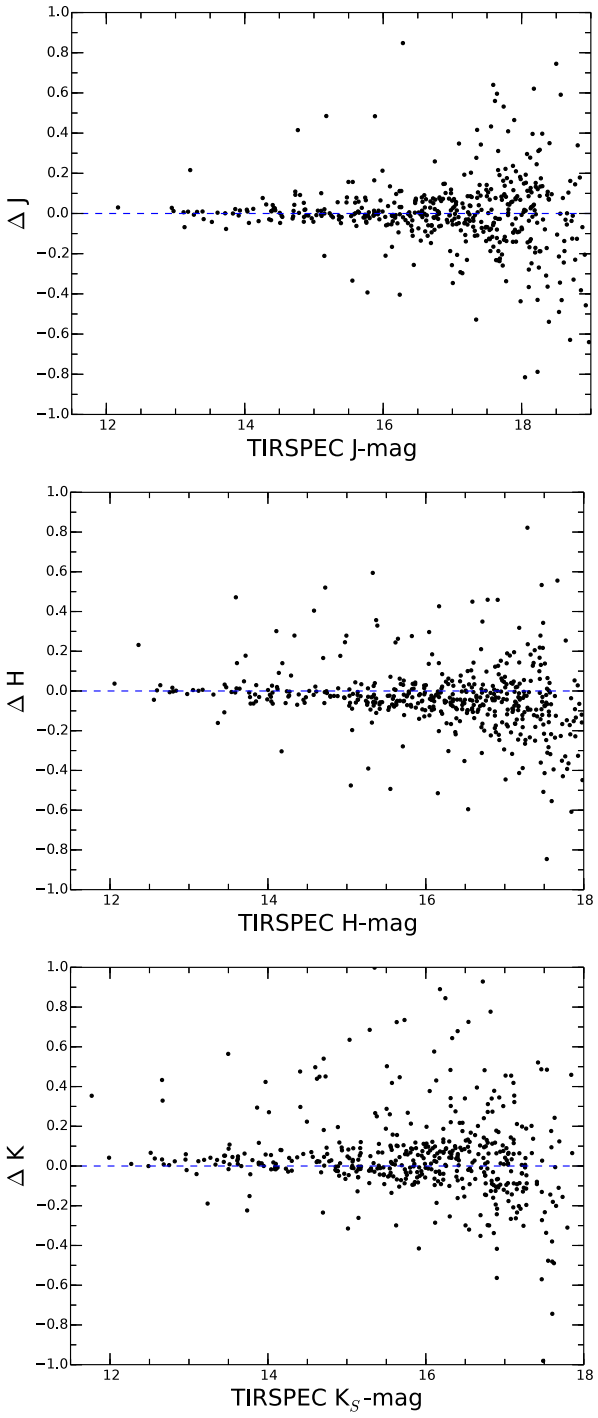

Figure 1. A comparison of TIRSPEC and UKIDSS magnitudes. Abacissae in all three figures are TIRSPEC magnitudes and ordinates are differences between UKIDSS and TIRSPEC magnitudes of the respective filter.

3.2 *Spitzer* Infrared Spectrum

Spitzer Infrared Spectrograph (IRS) archival data of the central bright source in the Sh2-138 region were obtained using *Spitzer* Heritage Archive. The basic calibrated data (BCD) images (Program ID: 1417, AOR key: 13048064, PI: IRS team) were used to extract the spectrum in low resolution channel (ch0: 5-15 μm). The final spectrum is obtained using the SPICE package. The details of the extraction and reduction steps of IRS spectra are available in the *Spitzer*-IRS handbook[2] (version 5.0).

3.3 WISE data

We utilized the publicly available archival WISE[3] (Wright et al. 2010) images at 3.4 (W1), 4.6 (W2), 12 (W3), and 22 (W4) μm as well as the photometric catalog. The resolution is $6''$ for the first three bands and is $12''$ for the 22 μm-band. The AllWISE point source catalog for $4'.6\times4'.6$ area was obtained.

3.4 *Herschel* continuum maps

Herschel (Pilbratt et al. 2010) continuum maps were obtained at 70, 160, 250, 350, and 500 μm using $Herschel$ Science Archive (HSA). The resolutions of these bands are $5''.8$, $12''$, $18''$, $25''$, and $36''$, respectively. We selected the processed level2_5 MADmap images for the Photoconductor Array Camera and Spectrometer (PACS) 70 and 160 μm bands, and the Spectral and Photometric Imaging Receiver (SPIRE) extended images at 250, 350, and 500 μm bands, observed as part of the proposal name: OT2_smolinar_7. The 70–160 μm maps are calibrated in the units of Jy pixel^{-1}, while the images at 250–500 μm are in the surface brightness unit of MJy sr^{-1}. The plate scales of the 70, 160, 250, 350, and 500 μm images are 3.2, 6.4, 6, 10, and 14 arcsec pixel^{-1}, respectively. We obtained $15'\times15'$ maps at 70–500 μm centred on $IRAS$ source. However, the analysis of temperature and column density maps is presented only for $9'\times9'$ area.

3.5 SCUBA 850 μm continuum map

Sub-mm Common-User Bolometer Array (SCUBA; Holland et al. 1999) 850 μm continuum map (beam $\sim14''$) of the Sh2-138 region was obtained from the SCUBA legacy survey (Di Francesco et al. 2008). The observations were performed using the James Clerk Maxwell Telescope (JCMT). One can find more details about 850 μm map in the work of Di Francesco et al. (2008).

3.6 Radio continuum data

Radio continuum map at 1.4 GHz (beam size $\sim45''$) was obtained from the NRAO VLA Sky Survey (NVSS) (Condon et al. 1998) archive. We also utilized the Very Large Array (VLA) archival images at 4890 MHz (Project: AR0346) and 8460 MHz (Project: AR0304).

[2] http://irsa.ipac.caltech.edu/data/SPITZER/docs/irs/irsinstrumenthandbook/
[3] Wide Field Infrared Survey Explorer, which is a joint project of the University of California and the JPL, Caltech, funded by the NASA

3.7 JCMT HARP ^{13}CO ($J = 3 - 2$) data

^{13}CO ($J = 3 - 2$) (330.588 GHz; beam $\sim14''$) data were retrieved from the JCMT archive (ID: M08BU18; PI: Stuart Lumsden). The observations were obtained in position-switched raster-scan mode of the Heterodyne Array Receiver Program (HARP; Buckle et al. 2009). We utilized the processed integrated CO intensity map of the Sh2-138 region.

3.8 Bolocam 1.1 mm image

We have obtained Bolocam 1.1 mm continuum map of the Sh2-138 region. The effective FWHM Gaussian beam size of the image is $33''$ (Aguirre et al. 2011).

4 MORPHOLOGY OF THE REGION

4.1 A multi-wavelength view of the Sh2-138 region

The spatial distribution of warm and cold dust emission in the Sh2-138 region at large scale (size $\sim 15'.0\times15'.0$) is shown in Figure 2. The features in the 4.6–70 μm range trace the warm dust emission, while cold dust emission is traced in the 160–1100 μm continuum images. Figure 2 illustrates the spatial morphology of the region, and the filamentary features are highlighted based on a visual inspection of the 250 μm map (see curves in the 1100 μm image panel in Figure 2; hereafter *Herschel* filaments). All these filaments are several parsecs in lengths and appear to be radially emanating from the position of $IRAS$ source, revealing a 'hub-filament' morphology (e.g. Myers 2009).

The colour composite image made using $VIK_{\rm s}$ bands (V: blue, I: green, and $K_{\rm s}$: red) is shown in Figure 3. The NVSS 1.4 GHz radio contours are also superimposed on the image to show the extent of the ionized region. One can infer from this image that the radio emissions and NIR $K_{\rm s}$-band nebulosity are found around the bright source near the $IRAS$ source position. The diffuse nebulosity associated with the region is also seen in the NIR 3-colour image (see Figure 4; J: blue, H: green, and $K_{\rm s}$: red).

In Figure 5, we present continuum-subtracted narrow-band images ($H\alpha$: 0.6563 μm, $[Fe\ {\rm II}]$: 1.644 μm, H_2: 2.122 μm, and $Br\gamma$: 2.166 μm) and WISE 3.4 and 4.6 μm images of the Sh2-138 region. The diffuse emission features are clearly visible in the $H\alpha$ and $Br\gamma$ images, however the features present in the $[Fe\ {\rm II}]$ and H_2 maps are faint. We observed a spatial correlation of detected features in the $H\alpha$ and $Br\gamma$ images which are elongated in the northwest direction. The emissions detected in the $H\alpha$ and $Br\gamma$ maps trace the distribution of ionized emission in the region. NVSS radio contours (coarse beam) are also extended in the northwest direction. To enhance the faint features seen in the H_2 and $[Fe\ {\rm II}]$ maps, we have median filtered them with a width of 6 pixels and smoothened by 6 pixels $\times$ 6 pixels. The H_2 features are very faint in our image. However, we have shown the H_2 emission contours above the 1-σ background level to bring out the H_2 distribution towards the $IRAS$ source. A bipolar cavity-like feature is traced in the H_2 map (see Figure 5). One can also find the similar features near the $IRAS$ source in WISE 3.4 and 4.6 μm images. Earlier Qin et al. (2008) detected bipolar molecular ^{12}CO ($J = 2 - 1$) outflows towards the $IRAS$ source in this region. Hence, we suggest that these faint features seen in H_2 image are probably originated by shocks.

In Figure 6, we present the distribution of ionized emission, molecular ^{13}CO ($J = 3 - 2$) gas, and cold dust emission in the

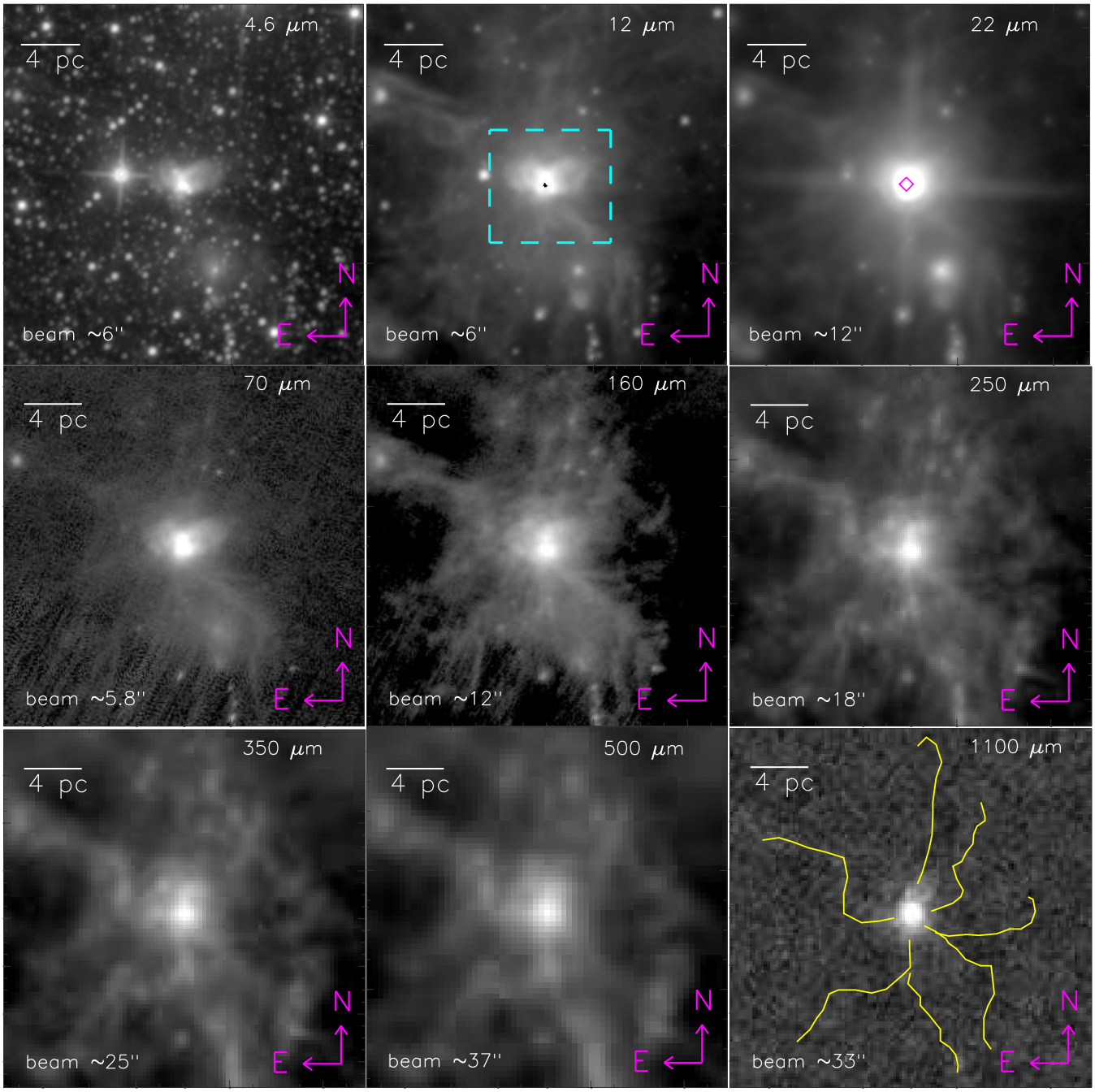

Figure 2. A multi-wavelength view (at large scale 15′ × 15′; central coordinates: α_{2000} = $22^h32^m45^s.26$, δ_{2000} = $+58°28'20''.97$) of the Sh2-138 region. The panels show images (at 4.6–1100 μm) from WISE (4.6–22 μm), *Herschel* Hi-GAL (70–500 μm), and BOLOCAM (1100 μm) (from left to right in increasing order). The scale bar on the top left shows a size of 4 pc at a distance of 5.7 kpc. The dashed cyan box in the panel of 12 μm image is shown as a zoomed-in view in Figure 3. The position of IRAS 22308+5812 is marked by a diamond symbol (◊) in 22 μm image. The 12 μm image is saturated near the $IRAS$ position. Filaments seen at 250 μm map are shown by yellow curves in the panel of the 1100 μm map (see the text for more details).

Sh2-138 region. Figure 6a shows GMRT 610 MHz radio contours (in yellow; beam $\sim 5''.5 \times 4''.8$) and 850 μm dust continuum contours (in cyan), overlaid on the $H\alpha$ image. The spatial distribution of ionized emission and $H\alpha$ emission is very well correlated. Figure displays that the peak position of 850 μm emission is shifted ($\sim 11''$) with respect to the peak position of 610 MHz radio emission.

The extent of molecular cloud associated with the Sh2-138 region is revealed in Figure 6b. In Figure 6b, we find two peaks of molecular gas in the integrated CO intensity map (i.e. northern and southern) and the $IRAS$ source is located close to the southern peak of CO map. In summary, the southern CO emission region is associated with the dust and radio continuum emissions.

All together, we find that the CO and dust condensation associated with the $IRAS$ source is located at the junction of filaments, where the signature of active star formation (i.e. outflow) is evident.

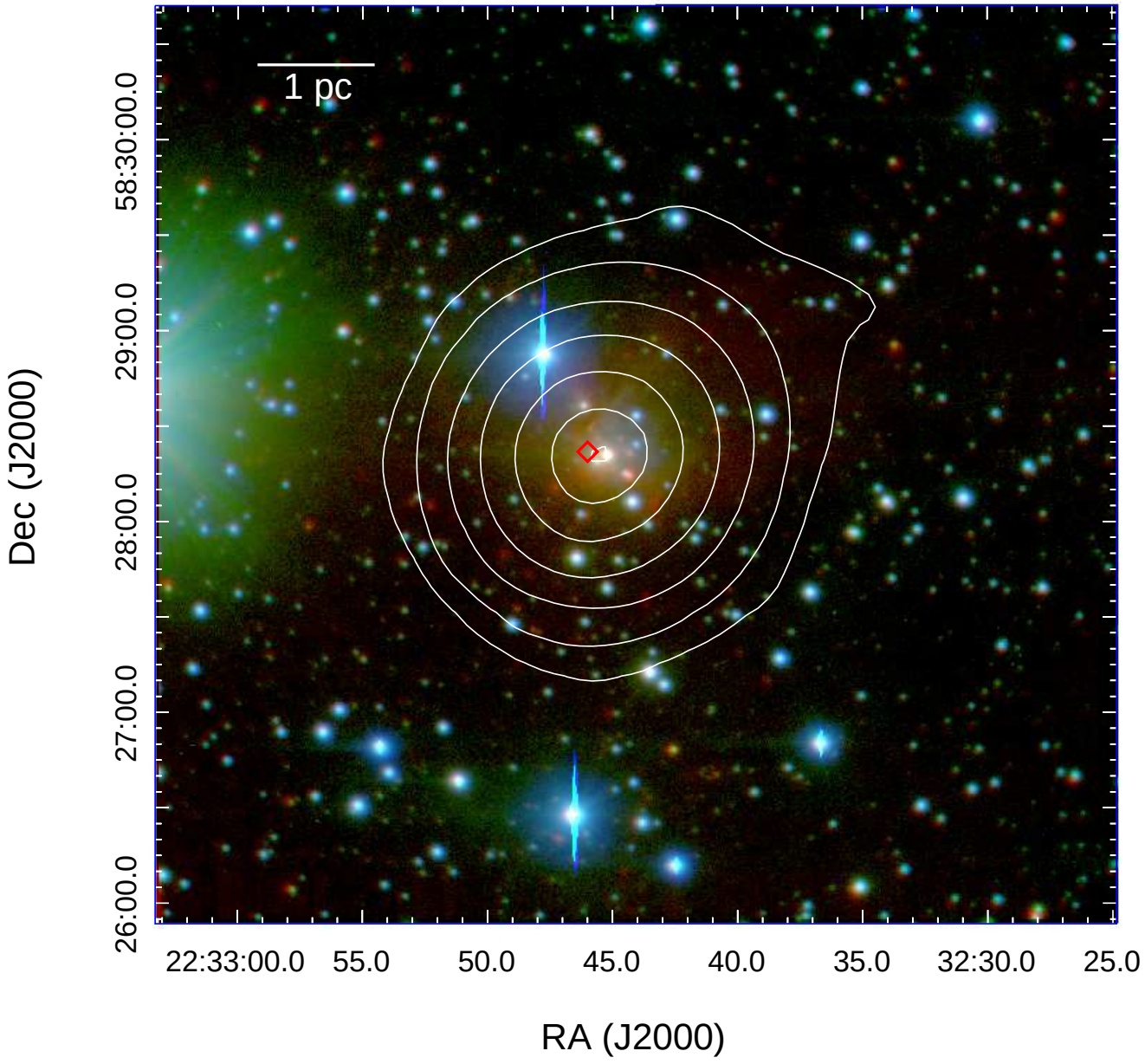

Figure 3. A 3-colour composite image of the Sh2-138 region (size of the selected field $4'.6 \times 4'.6$; central coordinates: α_{2000} =$22^h32^m44^s$, δ_{2000} = $+58°28'17''$). The image is the result of the combination of TIRSPEC NIR K_s-band in red, I-band in green, and V-band in blue. The area of this image is shown by a dashed box in Figure 2. Contours of NVSS 1.4 GHz radio emission in white colour are superimposed with 3σ, 20σ, 70σ, 200σ, 400σ, 650σ, and 850σ; where 1σ $\sim$1.56 mJy beam^{-1}. The position of IRAS 22308+5812 is marked by a diamond symbol ($\Diamond$). The scale bar at the top-left corner indicates 1 pc at a distance of 5.7 kpc.

4.2 Radio morphology and physical parameters

The presence of H II region is traced using NVSS 1.4 GHz emission (see Figure 3), however NVSS radio map cannot provide more insight into the small-scale morphology of the Sh2-138 H II region due to coarse beam size. To examine the detailed compact features present in the H II region, we obtained high resolution GMRT radio maps at 610 MHz (beam $\sim 5''.5 \times 4''.8$) and 1280 MHz (beam $\sim 3''.4 \times 2''.3$ or 0.094 pc $\times$ 0.063 pc). The 610 MHz map was presented in Section 4.1. The radio continuum map at 1280 MHz is shown in Figure 7, which reveals at least five compact peaks (also referred as radio clumps in this work) that are designated as A, B, C, D, and E.

We estimated the Lyman continuum flux (photons s^{-1}) for all these five clumps using the radio continuum flux, following the equation given in Moran (1983):

$$S_{Lyc} = 8 \times 10^{43} \left(\frac{S_\nu}{mJy}\right) \left(\frac{T_e}{10^4 K}\right)^{-0.45} \left(\frac{D}{kpc}\right)^2 \left(\frac{\nu}{GHz}\right)^{0.1} \quad (1)$$

where S_ν is the integrated flux density, T_e is the electron temperature, D is the distance to the source, and ν is the frequency. In the calculation, we assumed that the region is homogeneous and spherically symmetric, and each clump is powered by a single zero age main-sequence (ZAMS) source. The flux density (S_ν) and the size of each clump were determined using the AIPS task

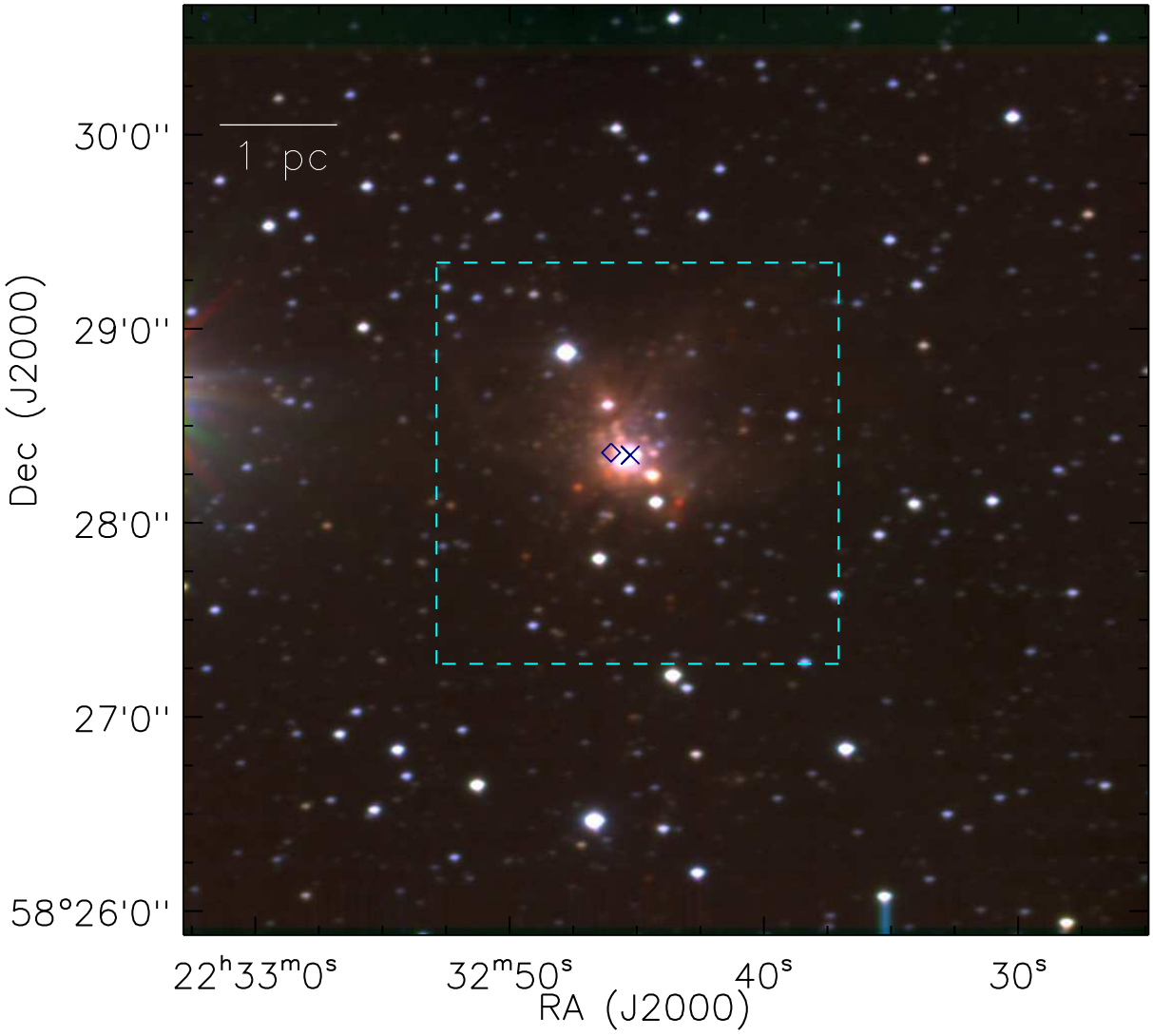

Figure 4. TIRSPEC NIR colour composite images (K_s-band: red, H-band: green, and J-band: blue) in log scale. The area of this image is shown by a dashed box in Figure 2. The position of IRAS 22308+5812 is marked by a diamond symbol (◊). A bright source, located at the centre, is marked by a '×' symbol. Optical, NIR, and MIR spectroscopic observations of this source are presented in Figures 11–14. One parsec scale bar is shown at the top-left corner, assuming distance to the region of 5.7 kpc. The dashed cyan box in the image is shown as a zoomed-in view in Figure 5.

JMFIT. The electron temperature, T_e, for these H II clumps was typically assumed to be 10^4 K, except clump 'A' (Stahler & Palla 2005). For clump 'A', T_e was found to be 9250 K using the model of Mezger & Henderson (1967) which is discussed in detail in the next paragraph. We estimated the spectral type of the powering star associated with each radio clump by comparing its Lyman continuum flux with the theoretical values given in Panagia (1973). The resultant spectral type of the powering star associated with each clump is given in Table 2. In Table 2, we have also listed 'clump name', clump peak position, observed frequency, integrated flux, size of the clump, and Lyman continuum flux. We find that four clumps (B, C, D, and E) are associated with sources of spectral type of B (earlier than B0.5V). The radio clump 'A' is ionized by an O9.5V type source, which is in agreement with previously estimated spectral type using 4.89 GHz flux by Fich (1993). A comparison of the GMRT 1280 MHz map, optical, and NIR images suggests that there are no optical and NIR counterparts found for four radio clumps (i.e. B, C, D, and E). However, the clump 'A' is found to be associated with at least three sources at the centre.

Note that the central compact clump 'A' is detected at four radio frequencies (i.e. GMRT 610 and 1280 MHz and VLA 4890 and 8460 MHz). Therefore, free-free emission spectral energy distribution (SED) fitting of the clump 'A' is performed to estimate its physical parameters (such as emission measure, electron density, Strömgren radius, and dynamical timescale). According to the model of Mezger & Henderson (1967), the flux density due to free-free emission arising in a homogeneous and spherically symmetric region can be written as:

$$S_\nu = 3.07 \times 10^{-2} T_e \nu^2 \Omega \left(1 - e^{-\tau(\nu)}\right) \quad (2)$$

$$\tau(\nu) = 1.643 \times 10^5 a T_e^{-1.35} \nu^{-2.1} n_e^2 l \quad (3)$$

where, S_ν is the integrated flux density in Jansky (Jy), T_e is the electron temperature of the ionized core in Kelvin, ν is the frequency in MHz, n_e is the number of electrons in cm^{-3}, l is the

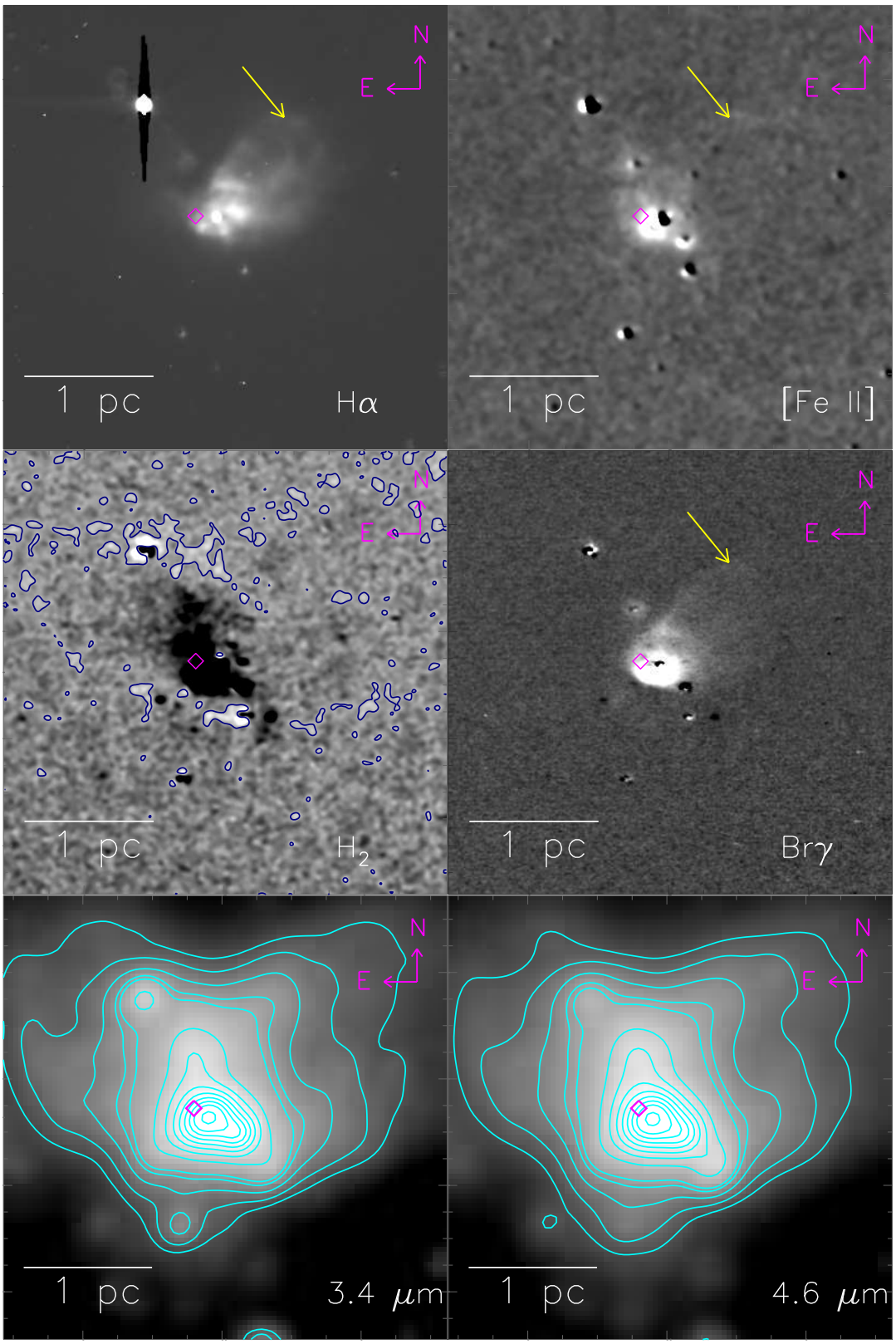

Figure 5. Continuum-subtracted narrow-band and WISE 3.4 and 4.6 μm images of the Sh2-138 region (size of the selected field $\sim 2'.07 \times 2'.07$; centered at α_{2000} = 22^h 32^m 45^s, δ_{2000} = +58° 28′ 18″.4). The area of these images is shown by a dashed box in Figure 4. Top left: $H\alpha$, top right: $[Fe\ II]$, middle left: H_2, middle right: $Br\gamma$, bottom left: WISE 3.4 μm, and bottom right: WISE 4.6 μm. WISE 3.4 and 4.6 μm contours are overplotted with the levels of 2, 3, 5, 8, 10, 20, 30, 40, 50, 60, 70, 80 and 95 % of the peak values on the respective images. In all the panels, diamond symbol (◊) marked the position of $IRAS$ source as shown in Figure 4. The yellow arrows represent the detected faint features in the region. In order to enhance the faint features, the H_2 and $[Fe\ II]$ maps are subjected to median filtering with a width of 6 pixels and smoothened by 6 pixels × 6 pixels. We have also drawn contours on H_2 image, above 1-σ background level to bring out the faint features seen in the image. The scale bar indicates 1 pc at a distance of 5.7 kpc.

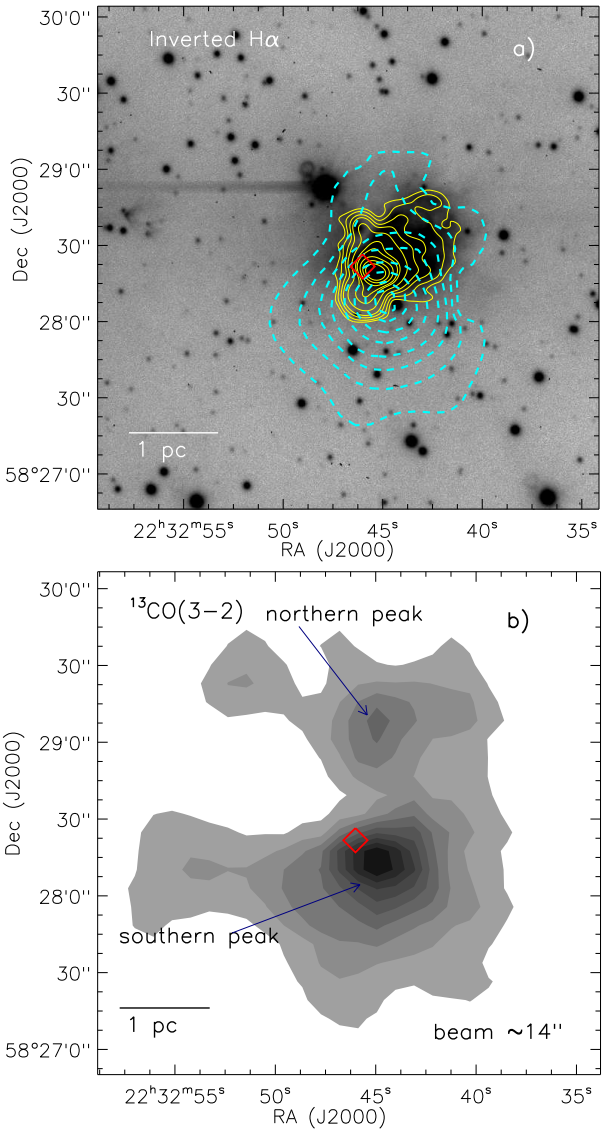

Figure 6. The distribution of dust emission, molecular gas, and ionized emission in the Sh2-138 region. a) Overlay of GMRT 610 MHz radio contours (yellow lines) and SCUBA 850 μm contours (dashed cyan lines) on the inverted grey-scale $H\alpha$ image (size of the selected field $3'.3 \times 3'.3$; central coordinates: α_{2000} =$22^h32^m46^s.7$, δ_{2000} = $+58°28'25''$). The 610 MHz radio contours are drawn at 12σ, 25σ, 50σ, 80σ, 150σ, 250σ, 300σ, 400σ, 500σ, and 600σ, where 1σ ~74.0 μJy beam^{-1}. SCUBA 850 μm contours are also overlaid on the image with the levels of 2.572 Jy/beam × (0.1, 0.2, 0.3, 0.4, 0.55, 0.7, 0.85, 0.95). b) The contour map of integrated JCMT-HARP ^{13}CO ($J = 3 - 2$) emission in the range of −58 to −45 km s^{-1}. The contour levels are 10, 20, 30, 40, 50, 60, 70, 80, and 90% of the peak value (i.e. 62.2 km s^{-1}). In both the panels, the other marked symbol is similar to that shown in Figure 4.

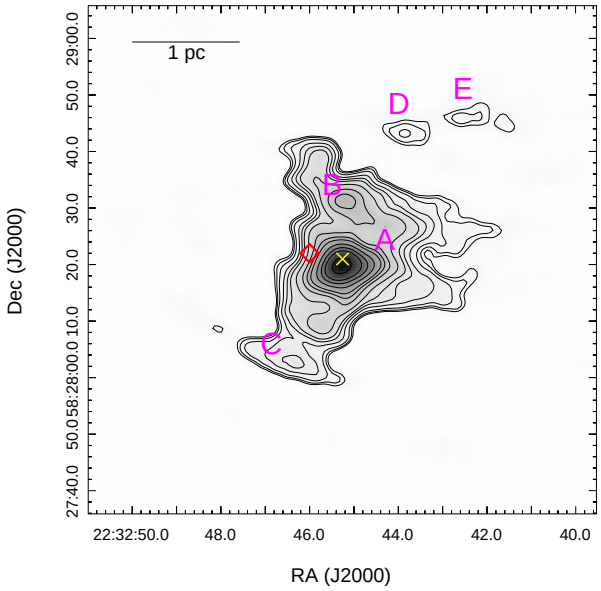

Figure 7. The high resolution GMRT radio continuum contours map at 1280 MHz (beam ~$3''.4 \times 2''.3$). The contours are shown with levels of 12σ, 15σ, 20σ, 30σ, 40σ, 50σ, 70σ, 100σ, 125σ, 150σ, 200σ, 250σ, 300σ, and 400σ, where 1σ ~71.7 μJy/beam. The 1280 MHz map traces at least five peaks, which are marked by A, B, C, D, and E (see Table 2).

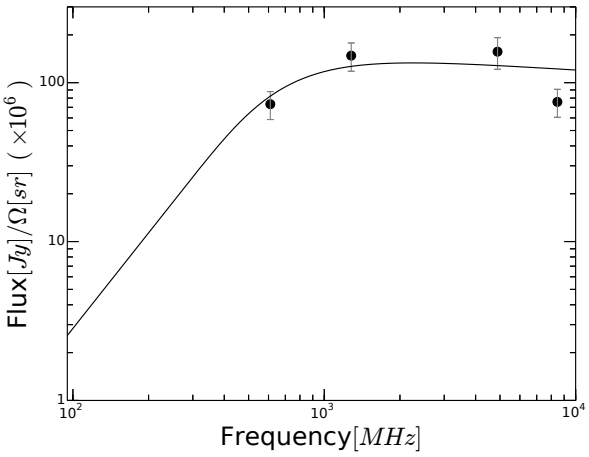

Figure 8. Radio SED of the central radio clump ('A'). Black filled circles are the flux densities at 610, 1280, 4890, and 8460 MHz. The error bars are shown for a ±10% error limit. The black curve is the model fit to the flux values. The fluxes at 610 and 1280 MHz are obtained from GMRT and the remaining two points are taken from VLA.

extent of the ionized region in parsec, τ is the optical depth, a is the correction factor, and Ω is the solid angle subtended by the source in steradian. The parameter $n_e^2 l$ represents the emission measure (in cm^{-6} pc), which is a measure of optical depth of the medium. In the calculations, we adopted the value of a = 0.99 (Mezger & Henderson 1967). The observed radio fluxes of clump 'A' were fitted by treating the temperature and emission measure as free parameters (similar to Omar, Chengalur & Roshi 2002; Vig et al. 2014). The model fit is sufficient to converge rapidly if observations are available at least one at optically thick regime (like 610 MHz) and another one at optically thin regime (like 4890 MHz). A chi-square minimization method was used in the fit to get the best estimate of the free parameters. The best fitted model returned a temperature of 9250±2000 K and an emission measure of 1.48±0.40×10^6 cm^{-6}pc (see Figure 8).

The knowledge of emission measure value and the linear extent (l) of the clump allows to estimate its electron density. The radio clump is comparatively more optically thin at 8460 MHz than other three observed radio frequencies. To obtain a better estimate of the extent of the clump, we calculated its linear extent (l) at 8460 MHz map, assuming a spherical morphology. The physical

extent of the clump was found to be 0.29±0.05 pc for a distance of 5.7±1.0 kpc. Finally, the electron density was estimated to be 2250±400 cm^{-3}. Earlier, Felli & Harten (1981) also obtained an electron density of 2500 cm^{-3} for this H II region using the flux at 4.99 GHz. Following the values tabulated in Kurtz (2002), our estimates of electron density (∼2250 cm^{-3}) and of the linear extent of clump (∼0.29 pc) correspond to a compact H II region.

The central massive source ionizes the surrounding medium and the ionization front expands until an equilibrium is established between the number of ionization and recombination. Theoretical radius of the H II region, called as Strömgren radius (Strömgren 1939), assuming a uniform density and temperature, is given by:

$$R_S = \left(\frac{3S_{Lyc}}{4\pi n_0^2 \beta_2}\right)^{1/3} \quad (4)$$

where R_S is the Strömgren radius, n_0 is the initial ambient density, and β_2 is the total recombination coefficient to the first excited state of hydrogen atom. The β_2 value for a temperature of 10^4 K is 2.60×10^{-13} cm^3 s^{-1} (Stahler & Palla 2005).

During the second phase of the expansion of the H II region, a shock front is generated because of high temperature and pressure difference between the ionized gas and the surrounding cold material. This pressure gradient allows the shock front to propagate into the surroundings. When this phenomenon occurs, the radius of the ionized region at any given time can be written as (Spitzer 1978):

$$R(t) = R_S\left(1 + \frac{7c_{II}t}{4R_S}\right)^{4/7} \quad (5)$$

where c_{II} is the speed of sound in H II region, which is assumed to be 11×10^5 cm s^{-1} (Stahler & Palla 2005). The calculated age of the region is highly dependent on the initial value of the ambient density. Therefore, in Figure 9, we plotted the variation of the Strömgren radius and the age with ambient density, from 1000 to 10000 cm^{-3} (e.g. classical to ultra-compact H II regions; Kurtz 2002), for the central clump 'A'. It can be seen in the figures that the Strömgren radius and the age vary from 0.33 to 0.07 pc and from 0.16 to 0.54 Myr, respectively. It is to be noted that in the calculation of Strömgren radius and dynamical age, the clump 'A' is commonly assumed to be homogeneous and spherically symmetric which might not be always true. Also, the region is far enough to have unresolved companion(s) and hence, there might be contribution of Lyman continuum photons from those unresolved embedded massive stars in the cluster. Hence, the above calculated values (dynamical age and Strömgren radius) can be considered as representative values for the clump 'A'.

4.3 Dust temperature and column density maps of the region

In this section, we present the temperature and column density maps of the Sh2-138 region, generated using *Herschel* images. Following the same procedures as described in Mallick et al. (2015), we generated the final temperature and column density maps by SED modeling of the thermal dust emission. In general, *Herschel* 70 μm emission comes from UV-heated warm dust, and therefore the 70 μm image is not used here. We adopted the following procedure to obtain the maps using *Herschel* 160–500 μm fluxes. First, we transformed all the images into the same units (i.e. Jy pixel^{-1}), and then convolved the images to the resolution and pixel scale of the 500 μm image (∼36″ resolution, 14″ pixel^{-1}) as it is the lowest among all the images. The background fluxes (I_{bg}), estimated from a relatively dark and smooth patch of the sky, were found to be 0.066, 0.493, 0.297, and 0.127 Jy pixel^{-1} for the 160, 250, 350, and 500 μm images (area of the selected region ∼5.′8×5.′8; central coordinates: α_{2000} ∼ 22$^{\rm h}$31$^{\rm m}$17$^{\rm s}$, δ_{2000} ∼ +58$^{\rm d}$32$^{\rm m}$09$^{\rm s}$), respectively. Finally, modified blackbody fitting was carried out on a pixel-by-pixel basis using the formula (Battersby et al. 2011; Sadavoy et al. 2012; Nielbock et al. 2012; Launhardt et al. 2013):

$$S_\nu(\nu) - I_{bg}(\nu) = B_\nu(\nu, T_d)\Omega(1 - e^{-\tau(\nu)}) \quad (6)$$

with optical depth formulated as:

$$\tau(\nu) = \mu_{H_2} m_H \kappa_\nu N(H_2) \quad (7)$$

where $S_\nu(\nu)$ is the observed flux density, I_{bg} is background, $B_\nu(\nu, T_d)$ is the modified Planck's function, T_d is the dust temperature, Ω is the solid angle subtended by a pixel, μ_{H_2} is mean molecular weight, m_H is the mass of hydrogen, κ_ν is the dust absorption coefficient, and $N(H_2)$ is the column density. In the calculations, we used Ω = 4.612×10^{-9} steradian (i.e. for 14″×14″ area), μ_{H_2} = 2.8 and κ_ν = 0.1 $(\nu/1000\ \mathrm{GHz})^\beta$ cm^2 g^{-1}, including a gas-to-dust ratio (R_t =) of 100, with a dust spectral index of β = 2 (see Hildebrand 1983). The resultant column density and temperature maps of the Sh2-138 region (angular resolution ∼36″; size ∼ 8′ × 8′) are shown in Figure 10. *Herschel* filaments are also shown in Figure 10. An isolated peak can be seen in the column density map (Figure 10b), whose corresponding temperature from the temperature map is ∼30 K. To estimate the clump mass, we used the 'clumpfind' software (Williams, de Geus & Blitz 1994) for measuring the total column density and the corresponding area of the clump seen in the column density map. The clump area was estimated to be ∼32 pc^2 (∼218 pixels, where 1 pixel corresponds to ∼0.382×0.382 pc^2), with a total column density of $\sim1.16\times10^{24}\ cm^{-2}$. The mass of the clump can be estimated using the formula:

$$M_{clump} = \mu_{H_2} m_H Area_{pix} \Sigma N(H_2) \quad (8)$$

where μ_{H_2} is assumed to be 2.8, $Area_{pix}$ is the area subtended by one pixel, and $\Sigma N(H_2)$ is the total column density estimated using 'clumpfind'. Using these values, we obtained the total mass of the clump to be ∼3770 M$_\odot$. Such a large clump mass has been reported earlier in other massive star-forming regions, like M17 (distance ∼1.6 kpc; Reid & Wilson 2006) and NGC 7538 (distance ∼ 2.8 kpc; Reid & Wilson 2005).

In addition to the clump mass, the average visual extinction towards the region was also estimated from the column density value using the relation $\langle N(H_2)/A_V\rangle = 0.94 \times 10^{21}$ molecules cm^{-2} mag^{-1} (Bohlin, Savage & Drake 1978) and assuming that the gas is in molecular form. We calculated an average column density of $\sim3.0\times10^{21}\ cm^{-2}$ (in the central 5′×5′ part of the column density map), which corresponds to visual extinction of A_V ∼3.2 mag. This agrees well with the extinction value towards the region found in literature (A_V ∼2.8 mag in Deharveng et al. 1999).

5 SPECTRAL TYPE OF THE CENTRAL BRIGHT SOURCE

As mentioned earlier, the radio clump 'A' appears to be associated with at least three point sources including a bright optical and infrared source. In order to determine the spectral type of this central bright source, we present its optical, NIR, and $Spitzer$-IRS spectra in this section. In the slitless $H\alpha$ spectra (see Section 2.2.1), we identified two sources with enhanced $H\alpha$ emission including the central bright source.

Table 2. Properties of the five radio clumps detected in GMRT 1280 MHz high resolution radio map.

Clump	RA (J2000) (deg)	Dec (J2000) (deg)	Obs. freq. (MHz)	Integrated flux (mJy)	Size	log (S_{Lyc}) (photons/sec)	Sp. type
A	338.188500	58.472133	610.0	390.01±0.66	14.″7×13.″6	48.000	O9.5
			1280.0	276.74±0.63	9.″5×7.″4	47.883	O9.5
			4890.0	310.53±0.73	9.″2×8.″1	47.991	O9.5
			8460.0	369.31±0.50	14.″8×12.″4	48.090	O9.0
B	338.188083	58.475247	1280.0	97.33±0.69	10.″6×7.″3	47.414	B0
			4890.0	46.08±0.83	11.″7×7.″5	47.147	B0
C	338.193125	58.467680	1280.0	39.46±0.78	13.″2×7.″7	47.022	B0
D	338.182417	58.478711	1280.0	9.94±0.50	10.″2×5.″3	46.423	B0.5
E	338.176750	58.479464	610.0	11.65±0.42	14.″5×8.″1	46.460	B0.5
			1280.0	7.51±0.44	11.″3×4.″1	46.301	B0.5

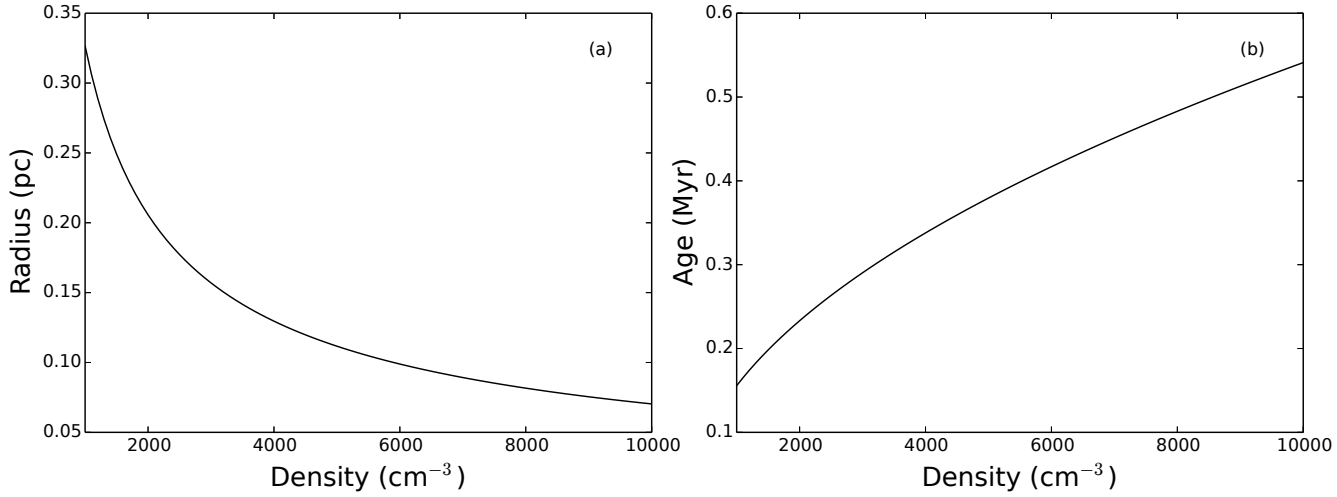

Figure 9. a) Figure shows the variation of the Strömgren radius with ambient density. b) Figure shows the variation of the dynamical age of the H II region with ambient density.

5.1 Optical spectrum

The observed optical spectrum of the central bright source (5000-9200 Å) is shown in Figure 11. The spectrum is corrected for the nebular emission, which was obtained by averaging the spectra adjacent to the source spectrum, assuming that the density of the nebular emission region is uniform. Apart from the strong hydrogen recombination lines, emission lines of He I at 5876 Å & 6678 Å, [O I] at 6300 Å & 6346 Å, [N II] doublet at 6548 Å & 6584 Å, [S II] doublet at 6717 Å & 6731 Å, and Ca II triplet at 8498 Å, 8542 Å, & 8662 Å are also seen in the spectrum. Presence of forbidden lines of [O I] at 6300 & 6364 Å, and [S II] at 6717 & 6731 Å is generally seen in the spectra of Herbig Ae/Be stars and their low-mass counterparts (i.e. classical T Tauri stars (CTTS)). These forbidden lines are often used to infer the presence of jets/outflows associated with the sources and originate only in low density conditions. Therefore, these lines are good tracers of excited low density material like jets/outflows (Finkenzeller 1985; Corcoran & Ray 1998).

The optical spectrum of the central bright source is similar to the spectrum of a Herbig Be star, MWC 137 (see Hamann & Persson 1992). These authors studied a total of 32 Herbig Ae/Be stars and found the Ca II triplet lines to be present in 27 sources, which is much higher than the detection rate in classical Be stars (∼20%). They also measured the equivalent widths of several characteristic lines of K, Fe, Mg, and Ca. In the case of MWC 137, the ratio of the equivalent widths of Ca II 8542 Å to 8498 Å lines was reported to be 1.16. It can be seen in our spectrum (Figure 11) that the Ca II triplet lines are blended with the Paschen series lines. To get an estimate of the pure contributions of Ca II triplet lines, we first subtracted the contribution of the Paschen series lines' fluxes assuming a Gaussian profile, and then measured the equivalent width of the Ca II lines. All the hydrogen recombination lines are originated at the same part of the gas and hence, expected to have same velocity broadening. Gaussian profiles subtracted from blended lines were generated by keeping the velocity constant as it is obtained from isolated recombination lines. In this work, the ratio of equivalent widths of Ca II 8542 Å to 8498 Å lines is found to be 1.2±0.3. The equivalent width ratios of O I 8446 Å to 7773 Å lines, and He I 5876 Å (blended) to 7065 Å are 3.0±0.3 and 1.5±0.2, respectively. The ratio of the equivalent widths of these characteristic lines is dependent on the spectral type of the source, i.e, whether Herbig Ae star or Be star

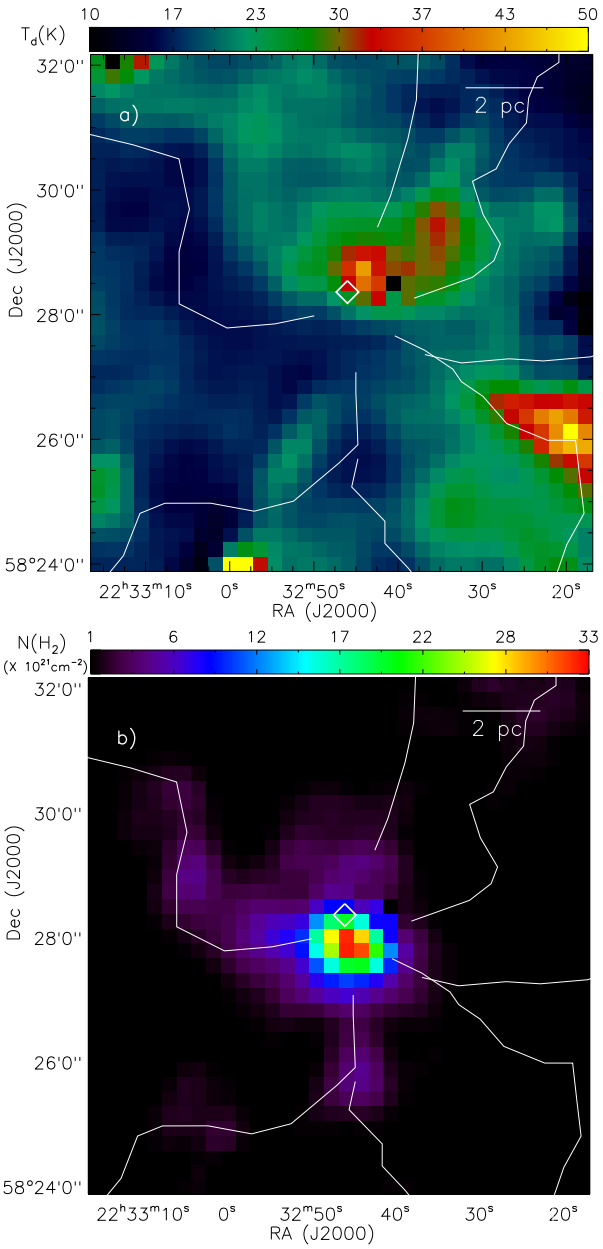

Figure 10. a) *Herschel* dust temperature and b) column density ($N(\mathrm{H_2})$) map of the Sh2-138 region (see text for details). The map also provides the information of extinction with $A_V = 0.94 \times 10^{-21}\ N(\mathrm{H_2})$. The *Herschel* filaments (see Figure 2) are also overplotted by solid curves in both the panels. The other marked symbol is similar to that shown in Figure 4.

(Hamann & Persson 1992). The analysis of optical spectra suggests that the central bright source is possibly a Herbig Be star.

We also estimated the electron density of the region from the ratio of [S II] 6716 Å to 6731 Å lines by comparing with the values given in Canto et al. (1980). The [S II] 6716 Å to 6731 Å line ratio for our spectrum is 1.0±0.1, which corresponds to an electron density of ∼500±300 cm^{-3} (also see Osterbrock & Ferland 2006), assuming a temperature of 10000 K (from Stahler & Palla 2005). Earlier, from their observed optical spectrum, Deharveng et al. (1999) had shown a variation of the electron density from 1000-200 cm^{-3} from the immediate vicinity of the central bright source to the outer part of the nebula. Martín-Hernández et al. (2002) also calculated the electron density of this region to be 768^{+366}_{-207} cm^{-3} using the [O III] 53 and 88 μm lines' ratio from the ISO spectrum. The electron density of this region determined using the optical/infrared spectrum is always found to be lower than the electron density estimated from the radio analyses (2250±400 cm^{-3} by us and ∼2500 cm^{-3} by Felli & Harten (1981)). However, the reason why the electron density value derived from optical/infrared spectrum is consistently lower than the value derived from radio analysis is not clear.

5.2 *Spitzer*–IRS spectrum

We present the $Spitzer$-IRS spectrum (5-15 μm) of the central bright source in Figure 13. The emission lines of [Ne II] and [Ar II–III] are seen in the spectrum, which suggest a presence of high energy photons in the circumstellar environment because the ionization of Ne and Ar, to the level of Ne II and Ar II–III, requires high energy photons ($>$ 21 eV). These highly energetic UV/X-ray photons generally originate at the stellar chromosphere or accretion shocks from massive stars.

Apart from these ionized lines, several polycyclic aromatic hydrocarbon (PAH) emission lines are also seen in the spectrum. The relative strength of the PAH emission lines can be used to quantify the degree of ionization of the PAHs which further gives a clue about the incident radiation field and temperature. Generally, the ionized PAHs emit strongly at 6–9 μm regime compared to the emission at 10–13 μm range (Allamandola, Hudgins & Sandford 1999).

Sloan et al. (2005) searched for any dependence of PAH emission features on their ionization fraction using the $Spitzer$-IRS spectra of four Herbig Ae stars, and found that the ratios of 7.7 and 11.3 μm PAH features are correlated with the spectral types of sources in their sample. The ratio of 7.7 to 11.3 μm PAH features was found to be 7.4 and 25.2 for spectral types of A0Ve and A5Ve, respectively, which implies a trend of decrease in ratio of PAH features for earlier spectral types of Herbig stars. For comparison, we have also measured fluxes at 7.7 μm and 11.3 μm PAH emission features from the $Spitzer$-IRS spectrum of our source and obtained fluxes of 43.2×10^{-15} Wm^{-2} and 9.9×10^{-15} Wm^{-2}, respectively. It is difficult to determine the continuum level separately for 7.7 and 8.3 μm PAH features. Sloan et al. (2005) had therefore included 8.3 μm PAH flux with 7.7 μm flux in their study. Following Sloan et al. (2005), we have also combined 8.3 μm PAH flux with the flux at 7.7 μm PAH feature to have a proper comparison. From the calculated flux, we obtained the ratio of fluxes at 7.7 and 11.3 μm PAH features to be ∼4.8, which is lower than the values reported for Herbig Ae stars in Sloan et al. (2005). It should be an indication that our source has an earlier spectral type than those four Herbig Ae stars reported in Sloan et al. (2005), and hence, has a lower ratio of 7.7 and 11.3 μm PAH features. We therefore suggest that the central bright source of the Sh2-138 region is possibly a Herbig Be star.

5.3 NIR spectra

The NIR ($YJHK$-band) spectra of the central bright source are shown in Figures 12 and 14. Prominent hydrogen lines are mainly seen in all the NIR spectra. Apart from the hydrogen recombination lines, strong He I line at 1.083 μm and its singlet counterpart at 2.058 μm is also present. As mentioned in Section 4.1, faint H_2 features are detected around the $IRAS$ source. Therefore, the rovibrational line of H_2 (1-0) at 2.122 μm is expected to be seen in

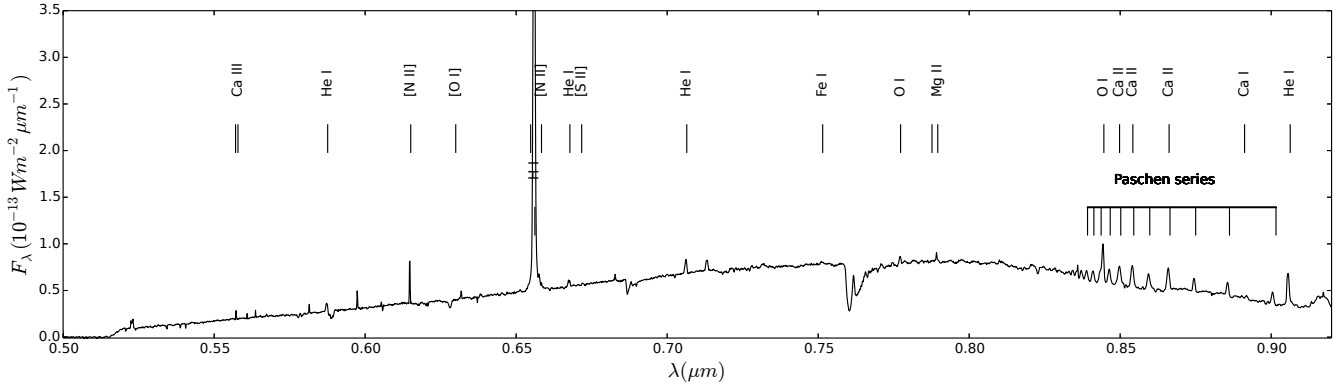

Figure 11. Optical spectrum of the central bright central source (marked by a '×' in Figure 4). Apart from the hydrogen recombination lines, several ionized lines of Ca & Mg and forbidden lines of [O I], [N II] & [S II] are also seen. The spectrum is similar to the spectrum of Herbig Be star, MWC 137

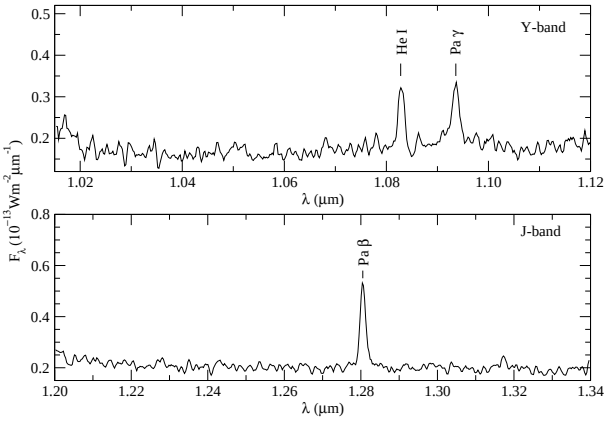

Figure 12. TIRSPEC NIR Y-band (top panel) and J-band (bottom panel) spectra of the central bright source (marked in Figure 4). Strong hydrogen lines and helium line at 1.083 μm are seen in the spectra.

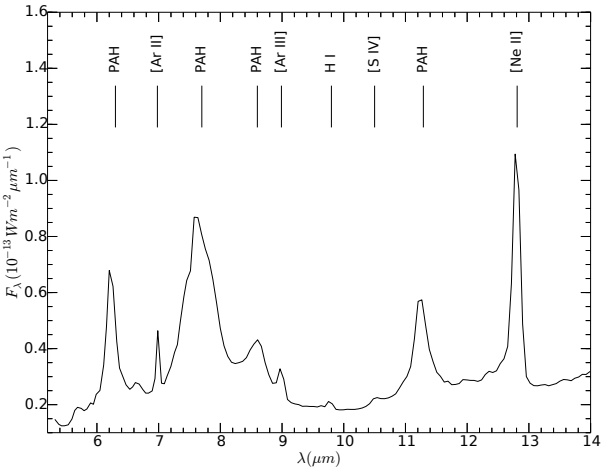

Figure 13. Low resolution (Channel 0) *Spitzer*-IRS spectrum of the central bright source (marked in Figure 4). Several PAH features and forbidden

the K-band spectrum. However, it is not detected possibly due to weak H_2 emission as seen in Figure 14.

A qualitative estimation for the spectral type of the central bright source is carried out following the methods described in Donehew & Brittain (2011). They performed UV, optical, and NIR spectroscopic study of 33 Herbig Ae/Be stars situated at different parts of the sky. They found a linear relationship between the accretion luminosity (L_{acc}) and the Brγ luminosity ($L_{Br\gamma}$) for Herbig Ae stars in their sample. The $L_{Br\gamma}$ was found to be higher for Herbig Be stars compared to Herbig Ae stars for the same value of L_{acc} (see Figure 3 in Donehew & Brittain 2011).

Donehew & Brittain (2011) calculated the accretion luminosity of their sources using the formula:

$$L_{acc} = \frac{GM_\star \dot{M}}{R_\star} \tag{9}$$

Where $M_\star$ is the stellar mass, $\dot{M}$ is the mass accretion rate, and $R_\star$ is the stellar radius. Following the same procedure, we estimated the L_{acc} of our source to be 5.3 $L_\odot$. In the calculation, we used the

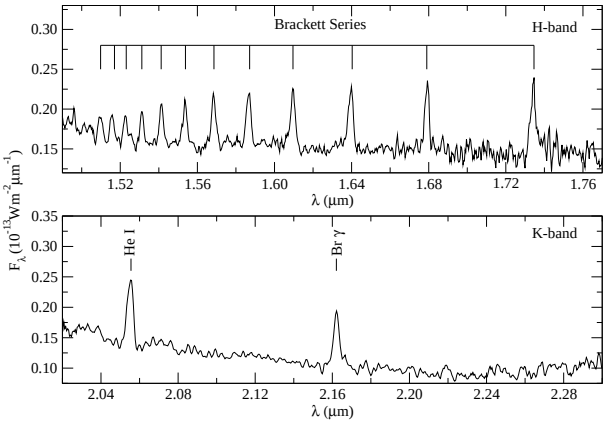

Figure 14. TIRSPEC NIR H-band (top panel) and K-band (bottom panel) spectra of the central bright source (marked in Figure 4). Strong Brackett lines are seen in both the spectra. Singlet counterpart of 1.083 μm He I line at 2.059 μm is also seen in the K-band spectrum.

SED derived physical parameters of the source (stellar mass = 9.1 $M_\odot$, mass accretion rate = 7.8×10^{-7} $M_\odot$ yr^{-1}, and radius = 47.8 $R_\odot$; see Section 6.3 for more details). We estimated the Brγ flux of the source from the K-band spectrum to be $6.15\pm0.3\times10^{-17}$ W cm^{-2}, which corresponds to a luminosity of 34 ± 10 $L_\odot$. In case of the sources listed in Donehew & Brittain (2011), we found that for an L_{acc} of $\sim$5.0 $L_\odot$, the ratio of L_{acc} to $L_{Br\gamma}$ is $\sim$5000 and $\sim$50 for CTTSs/Herbig Ae stars and Herbig Be stars, respectively. A further lower ratio of L_{acc} to $L_{Br\gamma}$ for our source ($\sim$0.16), implies that it should be at least a Herbig Be star.

From the overall view on the optical, NIR, and MIR spectra, we conclude that the central bright source is most-likely a Herbig Be star.

5.3.1 Extinction to the source

Prominent $Pa\beta$ and $Br\gamma$ lines are detected in emission in the NIR spectra of the central bright source located near the $IRAS$ source (see Figures 12 and 14). Hence, we used the observed ratio of these lines to estimate the extinction of the source. In order to infer the extinction value, we utilized the recombination theory and the observed flux ratio of $Pa\beta$ (1.282 μm) to $Br\gamma$ (2.166 μm). The intrinsic flux ratio of $Pa\beta$ to $Br\gamma$ (i.e. (Paβ/Brγ)$_{int}$ = 5.89) was obtained for Case B with T_e = 10^4 K and n_e = 10^4 cm^{-3} from Osterbrock & Ferland (2006). The differential reddening between $Br\gamma$ and $Pa\beta$ is given by, $A_\gamma - A_\beta = 2.5\log_{10}(Pa\beta/Br\gamma)_{obs} - 2.5\log_{10}(Pa\beta/Br\gamma)_{int}$. The extinction at 1.282 μm can be estimated using, $A_\beta = (A_\gamma - A_\beta)\,[(2.166\ \mu m/1.282\ \mu m)^{-1.9} - 1]^{-1}$ (e.g. Ho et al. 1990). We measured the ratio of $Pa\beta$ to $Br\gamma$ fluxes $(Pa\beta/Br\gamma)_{obs}$ of 1.68 from our NIR spectra (see Figures 12 & 14) and obtained A_γ = 0.8 mag and A_β = 2.16 mag using above relations. Subsequently, the visual extinction (A_V) of the source is estimated to be $\sim$7.0 mag using A_γ and the extinction law of Indebetouw et al. (2005). The deduced value of the extinction towards the central bright source is independent of distance. The difference between the foreground extinction (A_V $\sim$3.0 mag; see Section 6) and extinction towards this source indicates the presence of circumstellar material around the star.

6 YOUNG STELLAR POPULATION IN THE REGION

The study of young stellar sources and their distribution is important to understand the ongoing star formation in the region. In this section, we present the selection procedure of YSOs and analysis of their physical properties.

6.1 Selection of YSOs

We have identified YSOs in $4'.6\times4'.6$ area of the Sh2-138 region using three different methods: (1) the NIR $J-H/H-K$ colour-colour diagram (CC-D), (2) the NIR $K/(H-K)$ colour-magnitude diagram (CM-D), and (3) the WISE CC-D. These methods are discussed in greater details in the following sections.

6.1.1 NIR colour-colour diagram

In Figure 15, we show the NIR $J-H/H-K$ CC-D generated using the combined TIRSPEC and UKIDSS NIR catalog (see Section 3.1). The green curve in the CC-D represents the main-sequence (MS) locus, the solid blue curve is the locus of the giants (Bessell & Brett 1988), the blue dashed line shows the locus

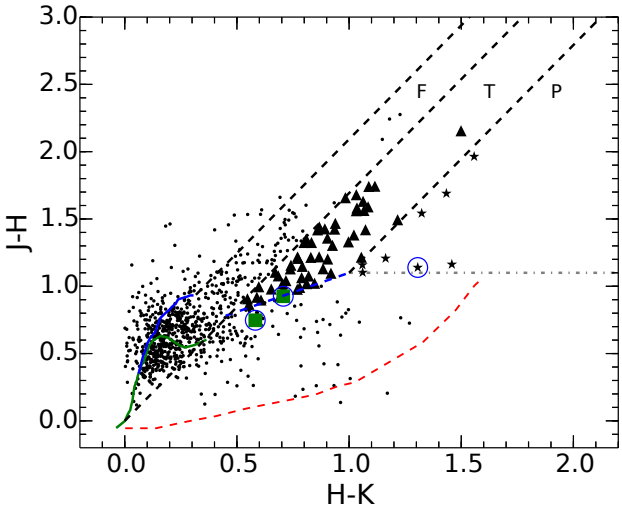

Figure 15. NIR CC-D ($H-K$ *vs* $J-H$) for the sources in the central $4'.6\times4'.6$ region of the Sh2-138. Solid triangles in the 'T' region and the asterisks in the 'P' region are Class II and Class I YSOs, respectively (see text). Two $H\alpha$ emission stars are marked by green squares. The solid curves represent the unreddened locus of MS dwarf stars (green) and giants (blue) (from Bessell & Brett 1988). The locus of the Herbig stars is shown in dashed red curve (Lada & Adams 1992), while the locus of CTTS stars is shown by a dashed blue line (Meyer, Calvet & Hillenbrand 1997), and the dashed-dotted grey line drawn at $J-H$ = 1.1 from the tip of the CTTS locus is to decrease the contamination of Herbig Ae/Be stars in the 'P' region. Three parallel black dashed lines are the reddening vectors drawn using the reddening laws from Cohen et al. (1981). Three sources, identified in our K_s-band image (marked by blue circle) are arranged in a Trapezium-like configuration (Deharveng et al. 1999).

of CTTS (Meyer, Calvet & Hillenbrand 1997), red dashed curve shows the locus of Herbig Ae/Be stars (Lada & Adams 1992) and the grey dashed-dotted line is drawn at $J-H$ = 1.1, extended from the tip of the CTTS locus. The parallel black dashed lines are the reddening vectors drawn from the base of the MS locus, turning point of the MS locus, and tip of the CTTS locus. All the magnitudes, colours, and loci of the MS, giants, CTTS and Herbig stars are converted to the Caltech Institute of Technology (CIT) system. The extinction laws A_J/A_V = 0.265, A_H/A_V = 0.155, A_{K_s}/A_V = 0.090 for the CIT system have been adopted from Cohen et al. (1981).

The sources in the CC-D (Figure 15) can be classified into three regions, namely, 'F', 'T', and 'P' (cf. Ojha et al. 2004a,b). The sources in the 'F' region are generally considered as evolved field stars or Class III YSOs (Weak-line T Tauri Stars). The sources in the 'T' region are mainly Class II YSOs (CTTS; Lada & Adams 1992) with a large NIR excess and reddened early type MS stars with excess emission in the K-band (Mallick et al. 2012). The sources in the 'P' region are Class I YSOs with circumstellar envelopes. There may be an overlap of Herbig Ae/Be stars with the sources in the 'T' and 'P' regions, which generally occupy the place below the CTTS locus in the NIR CC-D (for more detail see Hernández et al. 2005). Hence, to decrease any such contamination in the 'P' region, we have considered only those sources which have $J-H > 1.1$ mag. In this scheme, we have identified a total of 8 Class I and 53 Class II YSOs.

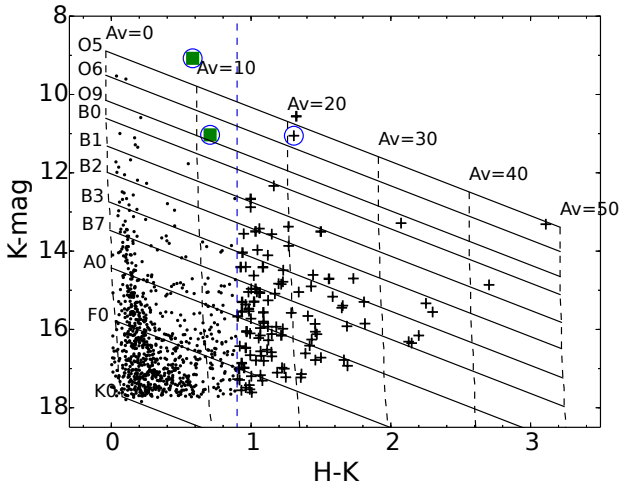

Figure 16. NIR CM-D ($K/H-K$) of the sources detected in both H- and K_s-bands. Solid slanting parallel lines show the reddening vectors corresponding to the spectral type indicated in the left. Nearly vertical solid lines show the ZAMS loci for a distance of 5.7 kpc with foreground extinction of A_v = 0, 10, 20, 30, 40 and 50 mag, respectively. The sources with infrared excess, marked with 'cross' symbols, are identified as candidate Class II/Class I YSOs. The cutoff value of $H-K \sim 0.9$ is shown by blue dashed line. The remaining symbols/colours are similar to those in Figure 15.

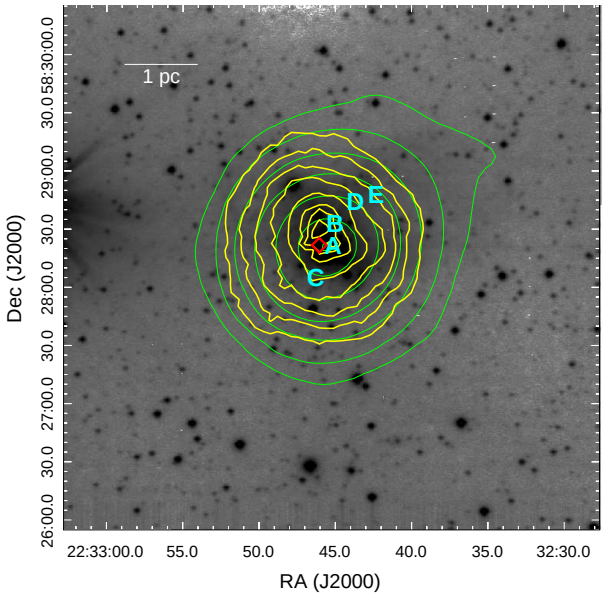

Figure 17. YSOs surface density contours of the Sh2-138 region calculated for 20NN overlaid on the NIR K_s-band image. The surface density contours (in yellow) are drawn at 5, 7, 10, 15, 25, 40, 50, and 60 YSOs pc^{-2}. We have also superimposed the NVSS 1.4 GHz radio contours (in green) at 3σ, 20σ, 70σ, 200σ, 400σ, 650σ, and 850σ; where σ ~1.562 mJy/beam. The positions of the clumps detected in the 1280 MHz radio map are marked by 'A', 'B', 'C', 'D', and 'E', and the other marked symbol is same as shown in Figure 4.

6.1.2 NIR colour-magnitude diagram

The NIR CM-D is a useful tool to identify a population of YSOs with infrared excess, which can be easily distinguishable from the MS stars. Figure 16 shows the NIR $K/H-K$ CM-D of the sources that are detected only in the H- and K-bands without any J-band counterparts. The CM-D of sources in the Sh2-138 region allows to identify additional YSOs. The black and red symbols in the CM-D are the same as used in the CC-D. Nearly vertical dashed black lines show the ZAMS loci for a distance of 5.7 kpc with foreground extinctions of A_V = 0, 10, 20, 30, 40, and 50 mag. The slanted parallel lines represent the reddening vectors for different spectral types, drawn using the extinction laws of Cohen et al. (1981).

It is to be noted that the UKIDSS catalog (H ~19.0; K ~18.0; Lucas et al. 2008) is deeper than the TIRSPEC catalog (H ~18.0; K ~17.8). Therefore, most of the faint and redder sources seen in the CM-D are observed only in the UKIDSS catalog.

In Figure 16, a low density gap of sources can be seen at $H-K \sim 0.9$ (marked by a blue dashed line). Therefore, red sources ($H-K > 0.9$) with infrared excess could be candidate Class II/Class I YSOs. The remaining sources with $H-K \leqslant 0.9$ are most-likely field stars. The colour criterion is consistent with the control field region (central coordinate: $\alpha_{2000} \sim 22^h32^m22^s$, $\delta_{2000} \sim +58^d33^m22^s$) where all the stars were found to have $H-K < 0.9$. Using the CM-D, a total of 114 sources have been detected as YSOs.

6.1.3 MIR colour-colour diagram

Additional YSOs are also identified using the WISE first three bands (W1, W2, and W3) magnitudes. The magnitudes with cc-flag of 'D', 'P', 'H', and 'O' (D: Diffraction spike; P: Persistence; H: Halo of nearby source; O: Optical ghost) for the first three bands were not considered in the analysis. We have removed the extragalactic sources, active galactic nuclei, shock objects, and PAH emission objects, following the colour criteria described in Koenig et al. (2008). Finally, we identified two Class I type and one Class II type YSOs from the WISE (W1-W2)/(W2-W3) CC-D.

The selected YSOs using the above three methods might have overlap among themselves and hence, the YSOs detected in the NIR CC-D and CM-D were matched first. While matching, priority was given to the YSOs identified in the NIR CC-D if the source is detected in both (as it is done in Mallick et al. 2013), because the CC-D, constructed using 3 band magnitudes, provides more robust information about the Class of YSOs. No NIR counterparts of the WISE YSOs were found in the combined catalog of YSOs identified using the NIR CC-D and CM-D. Finally, we have identified a total of 149 YSOs in 4′.6×4′.6 area (10 Class I, 54 Class II, and 85 infrared excess sources which could be candidate Class II/Class I YSOs), using the NIR CC-D or CM-D or MIR CC-D. The full catalog of YSOs is presented as supplementary material of this paper.

6.2 Surface density of YSOs

The surface density analysis of identified YSOs in the Sh2-138 region is performed using the nearest neighbor (NN) method (e.g. Casertano & Hut 1985; Schmeja, Kumar & Ferreira 2008; Schmeja 2011). We have performed 20NN surface density analysis because Monte Carlo simulations show that 20NN is adequate to detect cluster with 10 to 1500 YSOs (Schmeja, Kumar & Ferreira 2008). First, we divided the image (our selected 4′.6×4′.6 FoV) into a ~ 3″.7 (i.e. ~ 0.1 pc) regular grid. Subsequently, the distance to the 20^{th} YSO at each point of the grid (i.e. d_{20}) was measured and then, the area of the circle was calculated by taking the

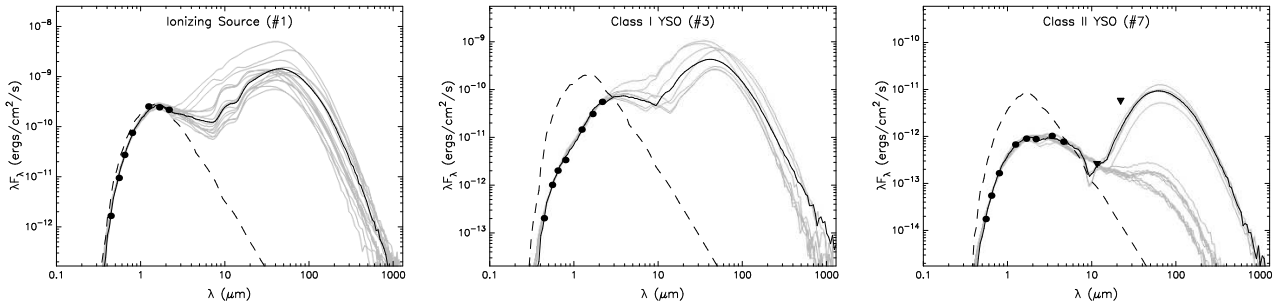

Figure 18. SED fitting for central brightest source (left), Class I (middle), and Class II (right) YSOs using the online tool of Robitaille et al. (2007) and their corresponding serial numbers in Table.3 are also written in the bracket. The black dots are the data points, while the black triangles are the upper limit of fluxes. The solid black line is the best fit to the data points and the grey lines show the consecutive good fits for $\chi^2 - \chi^2_{min} < 3$ (per data point). The dashed black line shows the best fit assuming that the observed fluxes are truly photospheric.

measured distance as a radius. Finally, the surface density of YSOs per pc^2 ($\frac{20-1}{\pi d^2_{20}}$) was estimated at each point of the grid. Figure 17 shows the spatial correlation between YSO surface density and ionized emission. In the figure, the surface density contours and 1.4 GHz radio continuum emission are distributed nearly symmetric, and centered on the massive source (associated with clump 'A'). Furthermore, the surface density map reveals an isolated cluster of YSOs in the Sh2-138 region, and all compact radio clumps seen at 1280 MHz are located within the cluster.

6.3 Spectral Energy Distribution

In this section, we present the results of SED modeling performed using an on-line SED modeling tool (Robitaille et al. 2006, 2007) for a selected subset of YSOs that have photometric fluxes available in at least 5 bands. The grids of YSO models, computed using the radiation transfer code of Whitney et al. (2003a,b), are explained in Robitaille et al. (2006, 2007). The models assume an accretion scenario with three different components - (1) a pre-main sequence central star, (2) a surrounding flared accretion disk, and (3) a rotationally flattened envelope with cavities. The model grid has a total of 200,000 SED models and each model covers a range of stellar masses from 0.1 to 50 $M_\odot$. In the SED fitter tool, these models try to find out the best possible match for the given fluxes at different wavelengths, following the chi-square minimization, with distance and interstellar visual extinction (A_V) as free parameters. The SED fitting tool requires at least three data points to model the observed SED, however the diversity of output model parameters can be constrained by providing more data points at longer wavelengths.

We selected 19 YSOs for the SED modeling that have detections in at least 5 bands. Additionally, 6 YSOs out of 19 have WISE fluxes. We treated these WISE fluxes as upper limits due to lower resolution. We used A_V in the range of 3–40 mag and our adopted distance to the Sh2-138 region of 5.7$\pm$1.0 kpc, as input parameters for SED modeling. The A_V range is basically taken from the average foreground extinction to the extinction of the reddest source detected in our catalog. We only selected those models which satisfy the criterion: χ^2 - $\chi^2_{best} < 3$, where χ^2 is taken per data point. Note that the output parameters of SED modeling are not unique, hence, the computed parameters should be taken as representative values. Therefore, the weighted mean value of model fitted parameters for 19 selected YSOs are computed. Figure 18 shows the example model fits for the central massive source, a Class I YSO, and a Class II YSO, respectively. All 19 model fitted SEDs are presented as supplementary material of this paper. The weighted mean values of the stellar age, stellar mass, disk mass, disk accretion rate, envelope mass, stellar temperature, total luminosity, and extinction for 19 YSOs are listed in Table 3. Additionally, table also includes the positions of sources and χ^2_{min} values.

We noticed that the age of majority of YSOs lies between 0.1 and 4 Myr, with a mean age of $\sim$1 Myr (see Table 3). Masses of YSOs show a range from 2 to 9 $M_\odot$ and majority of them (13 out of 19) have masses ranged between 2 and 6 $M_\odot$. Two sources have masses and ages $>$7 $M_\odot$ and $<$0.03 Myr, respectively, that are located in the central part of the cluster. The A_V of YSOs varies between $\sim$3 to 9 mag. Two $H\alpha$ emission stars and a Class I YSO show a high disk accretion rate of about 10^{-6} to 10^{-7} $M_\odot$ yr^{-1}.

6.4 Mass and Age spread from optical V/V-I colour-magnitude diagram

The $V/V-I$ CM-D of YSOs, which are detected in optical V- and I-bands, is shown in Figure 19. We have utilized optical photometry of YSOs to estimate their stellar mass and age. In general, the optical CM-D is a better tool to obtain stellar mass and age of YSOs than NIR CM-D, because optical fluxes of YSOs suffer less from their circumstellar emission than the fluxes in the NIR bands. In Figure 19, asterisks represent Class I YSOs, triangles represent Class II YSOs and crosses are sources with infrared excess identified in NIR CM-D. Though it is generally expected that Class I YSOs cannot be seen in optical bands, we have detected two of them possibly because they are located near the edge of 'P' and 'T' regions (see Figure 15) and with photometric uncertainty they can be either Class I or Class II YSOs. However, we left the nomenclature as Class I only, because technically they situated on the Class I side of the diagram. The green square symbols represent the enhanced $H\alpha$ emission sources which are detected in slitless $H\alpha$ spectra. In Figure 19, we have overplotted the ZAMS locus for solar metallicity as well as the pre-main-sequence (PMS) isochrones for 0.1, 0.5, 2.0 and 5.0 Myr (from Siess, Dufour & Forestini 2000). The evolutionary tracks of PMS stars for 0.3, 0.5, 1.0, 1.5, 2.0, 3.0, and 4.0 $M_\odot$ are also shown in Figure 19. All the isochrones, ZAMS locus and evolutionary tracks are corrected for a distance of 5.7 kpc and foreground extinction of A_V $\sim$3.0 mag.

A wide spread of ages and masses can be noticed in Figure 19. The sources with $H\alpha$ emission are found to be at age of $<$ 0.1 Myr, which are in agreement with the ages obtained from the SED modeling (see Table 3). The masses of majority of YSOs are found in the range from 0.4 to 4.0 $M_\odot$, which also agree well with the SED results. Note that we have corrected only the foreground extinc-

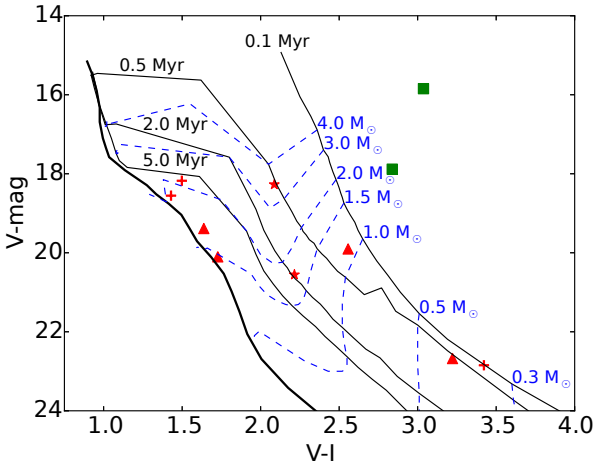

Figure 19. YSOs detected in both V- and I-bands are plotted. The symbols are same as shown in Figures 15 and 16 (asterisks: Class I YSOs; triangles: Class II YSOs; crosses: YSOs identified with infrared excess in NIR CM-D; green squares: sources with $H\alpha$ emission). Solid thick black line is the ZAMS locus, and thin black lines are PMS isochrones from 0.1–5 Myr adopted from Siess, Dufour & Forestini (2000). Blue dashed lines represent the evolutionary tracks for different masses. All the isochrones, ZAMS locus and evolutionary tracks are corrected for a distance of 5.7 kpc and foreground extinction of A_V ∼3.0 mag.

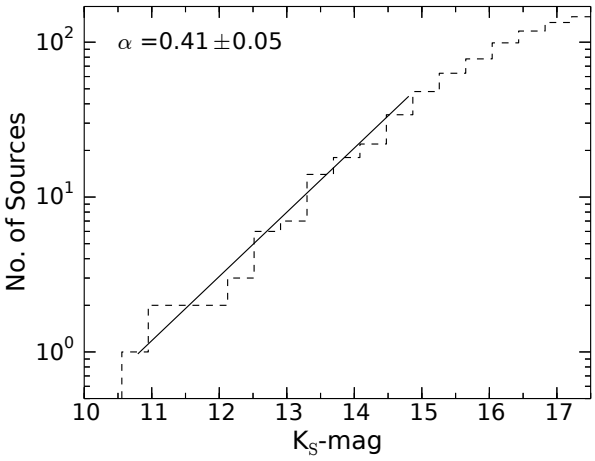

Figure 20. The completeness-corrected cumulative KLF for the YSOs binned in 0.5 mag. The black straight line is the fit to the KLF in 11–14.5 mag range and the corresponding slope is given by α.

tion for isochrones, however the extinction due to local clouds and circumstellar material can also cause apparent spread in age and mass. Similar age and mass spreads were reported in other star-forming regions like Sh2-297 (Mallick et al. 2012), young open cluster Stock 8 (Jose et al. 2008), and NGC 1893 (Sharma et al. 2007). However, determining the ages of PMS stars is a rather difficult task and the age-spread obtained in CM-D can be explained due to variable extinction towards the individual sources, photometric variability due to presence of disk/accretion, spatially unresolved binaries, and scattered light from the disk with large inclination (Hillenbrand, Bauermeister & White 2008; Soderblom et al. 2014).

6.5 The K_s-band Luminosity Function

An estimation of the age of a stellar cluster can be obtained from the K_s-band luminosity function (KLF; Zinnecker, McCaughrean & Wilking 1993; Lada & Lada 1995; Vig et al. 2014). As pointed out by Lada, Alves & Lada (1996), the age of a cluster can be estimated by comparing its KLF to the observed KLFs of other young clusters. In the calculation, we assume that the luminosity function for a stellar cluster follows a power law. Therefore, one can define the KLF as $d\mathrm{N}(K_s)/dK_s \propto 10^{\alpha K_s}$, where α is the slope of the power law. The KLF slope is estimated by fitting the cumulative number of YSOs in 0.5 K_s magnitude bin, which is significantly higher than the errors associated with K_s-band magnitudes. We corrected the magnitude bins with corresponding completeness factor (see Section 2.3) prior to fitting of the slope. In Figure 20, we show the completeness-corrected cumulative KLF of YSOs detected in the Sh2-138 region by dashed line, and the model fit to the KLF is shown by a solid line. The KLF is fitted for a magnitude range from 11.0 to 14.5 mag and the corresponding fitted slope is (α =) 0.41±0.05.

Similar values of α have been found by several authors in different high-mass star-forming regions. Recently, Mallick et al. (2014, 2015) obtained α of 0.40±0.3 and 0.35±0.4 for NGC 7538 (distance ∼2.65 kpc, age ∼1 Myr) and IRAS 16148-5011 (distance ∼3.6 kpc; age ∼1 Myr) star-forming regions, respectively. Earlier, Lada & Lada (1995) and Lada et al. (1991) also found similar value of α for the Orion molecular cloud (∼0.38, age ∼1 Myr). Comparable values of α are also found for several star-forming regions like, NGC 1893 cluster (∼ 0.34±0.07, distance ∼3.25 kpc; age ∼1-2 Myr; Sharma et al. 2007), and IRAS 06055+2039 cluster (∼0.43±0.09, distance ∼2.6 kpc; age ∼2-3 Myr; Tej et al. 2006). The age spread obtained for YSOs in the Sh2-138 region from the $V/V-I$ CM-D is similar to other massive star-forming region and the estimated KLF slope is in agreement with the slopes of several other young clusters. Noting the α values and ages of all these massive star-forming regions, we conclude that the mean age of the Sh2-138 cluster is possibly ∼1-2 Myr.

6.6 The stellar mass spectrum

In Section 6.4, we presented the mass and age spreads of YSOs using the $V/V-I$ CM-D. However, several YSOs identified in the Sh2-138 region do not have optical counterparts because of high extinction towards the region. Hence, we have constructed the NIR $J/J-H$ CM-D to obtain an estimate of the mass range for majority of YSOs. In the estimation of the stellar masses of YSOs using NIR magnitudes, only J- and H-bands were considered. The NIR K_s-band magnitude is not used in this analysis because the circumstellar material of YSOs emits strongly in K_s-band regime compared to J- and H-bands and hence, inclusion of K_s-band flux in this analysis might lead to an overestimation of the stellar mass. The $J/J-H$ CM-D of YSOs detected in both J- and H-bands is shown in Figure 21. We have overlaid ZAMS loci from Siess, Dufour & Forestini (2000) for A_V = 3.0 and 9.0 mag (see Section 6.3 and Table 3) and the evolutionary tracks for 0.5 and 4.0 $M_\odot$ PMS stars (Siess, Dufour & Forestini 2000) for both these extinction values. All the loci and tracks are corrected for a distance of 5.7 kpc. The YSOs selected for the SED modeling are marked with red circles, and the enhanced $H\alpha$ emission sources are shown with green squares. Most of the YSOs are found to be well distributed in the mass range from 0.5–4.0 $M_\odot$, with A_V ranged from 3.0–9.0 mag, which is consistent with the SED modeling results.

Table 3. SED model output parameters of selected YSOs.

Sr No.	RA (J2000) (deg)	Dec (J2000) (Deg)	Log (Age) (yr)	Mass ($M_\odot$)	log (M_{disk}) ($M_\odot$)	log ($\dot{M}_{disk}$) ($M_\odot yr^{-1}$)	log (M_{env}) ($M_\odot$)	log ($T_\star$) (K)	log (L_{tot}) ($L_\odot$)	A_V (mag)	χ^2 (per data points)
					$H\alpha$ emission stars						
1	338.188570	58.472493	4.45±0.10	9.10±0.34	-1.57±0.86	-6.11 ±0.86	1.31±0.54	3.73±0.03	3.23±0.08	4.36±0.38	3.27
2	338.190270	58.471976	4.94±0.34	5.62±1.06	-1.72±0.88	-7.16 ±1.21	0.53±0.89	3.69±0.06	2.35±0.24	4.03±0.75	2.93
					Class I YSOs						
3	338.185070	58.470722	4.41±0.01	8.13±0.01	-0.56±0.01	-5.25±0.01	0.61±0.01	3.67±0.01	2.89±0.01	3.00±0.01	2.84
4	338.193315	58.471851	5.07±0.01	6.80±0.01	-1.24±0.01	-6.61±0.01	0.50±0.01	3.70±0.01	2.71±0.01	4.66±0.01	3.43
					Class II YSOs						
5	338.140670	58.497884	6.51±0.01	6.41±0.01	-6.60±0.01	-13.02±0.01	-5.97±0.01	4.29±0.01	3.07±0.01	6.92±0.05	3.47
6	338.170170	58.474590	6.33±0.74	4.38±1.66	-5.27±2.10	-11.03±2.26	-3.97±2.99	4.02±0.19	2.26±0.46	8.44±1.14	0.09
7	338.170830	58.444609	5.07±0.01	2.08±0.01	-0.97±0.01	-6.64 ±0.01	0.03±0.01	3.64±0.01	1.58±0.01	4.72±0.01	4.66
8	338.171130	58.470674	5.46±1.06	4.06±2.68	–	–	-1.80±3.78	3.71±0.11	1.74±0.87	4.47±1.09	0.77
9	338.173390	58.444698	5.59±1.16	4.15±2.65	–	–	-2.21±3.65	3.81±0.18	1.95±0.67	5.24±1.62	0.09
10	338.194140	58.459910	6.62±0.38	3.20±1.18	-4.16±1.70	-9.77 ±1.72	-5.63±1.78	4.06±0.08	1.91±0.34	9.11±0.72	0.03
11	338.200690	58.486168	5.89±0.00	6.86±0.00	-2.09±0.00	-8.01 ±0.00	0.26±0.00	4.31±0.00	3.18±0.00	4.64±0.00	4.26
12	338.221150	58.468433	6.69±0.60	2.98±1.79	-3.15±1.27	-8.74 ±1.23	-4.16±2.63	3.98±0.06	1.65±0.52	3.97±0.41	6.83
13	338.238310	58.466403	5.82±0.67	4.06±1.28	-3.70±1.13	-9.15 ±1.41	-3.87±3.87	3.80±0.13	1.98±0.18	8.12±1.31	0.57
					YSOs with $H-K>0.9$						
14	338.184145	58.475136	6.15±0.03	3.62±0.06	-4.15±2.11	-10.27±1.87	-4.74±2.22	3.89±0.03	2.04±0.05	3.21±0.23	27.50
15	338.188256	58.449883	6.34±0.82	3.09±1.95	-4.62±1.18	-10.42±1.51	-3.77±3.08	3.87±0.12	1.53±0.56	4.28±0.96	7.56
16	338.211855	58.469717	5.10±0.99	5.64±3.25	-2.47±1.40	-7.63 ±1.96	-0.40±2.20	3.74±0.13	2.25±0.89	3.87±1.16	0.22
17	338.242297	58.478497	6.40±0.63	3.28±1.83	-4.18±2.31	-9.74 ±1.90	-4.39±3.49	3.89±0.04	1.75±0.67	3.43±0.39	3.52
18	338.245190	58.473235	4.54±1.09	6.54±1.60	-1.70±1.31	-6.49 ±0.87	0.60±0.08	3.74±0.12	2.73±0.34	4.99±1.83	4.92
19	338.252860	58.487277	6.35±0.45	3.68±1.23	-2.86±0.74	-8.97 ±0.86	-1.82±1.87	4.05±0.08	2.11±0.58	4.07±1.03	3.87

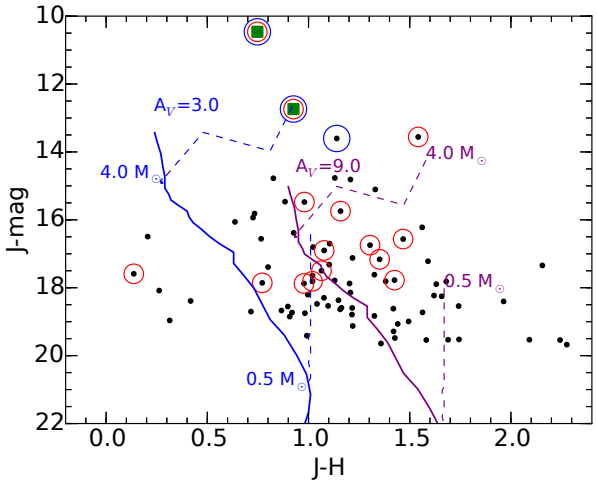

Figure 21. $J/J-H$ CM-D for the YSOs detected both in J- and H-bands (black dots). The solid blue and maroon curves show ZAMS loci from Siess, Dufour & Forestini (2000) for A_V of 3.0 and 9.0 mag, respectively. The evolutionary tracks for 0.5 and 4.0 M$_\odot$ PMS stars are also shown with dashed curves for both the extinction values. The selected YSOs for which SED analysis was performed are shown with additional red circles. The remaining symbols are similar to those shown in Figure 15.

7 DISCUSSION

Deharveng et al. (1999) discussed the stellar cluster in the Sh2-138 region using NIR data and compared it with the cluster found in the Sh2-106 region. Furthermore, they suggested that the presence of four massive stars, including a probable Herbig Ae/Be star in the central part of the Sh2-138 cluster, has a similar configuration to that found in the Orion Trapezium cluster. We found two among them are $H\alpha$ emission stars in our slit-less spectra. In our selected 4.′6×4.′6 area in the Sh2-138 region, a detailed analysis of stellar content suggests the presence of a cluster centered on the $IRAS$ source position which mainly contains low-mass stars along with a few embedded massive stars. The CM-D analysis ($J/J-H$) has revealed that most of the sources have masses from 0.5–4.0 M$_\odot$ for visual extinction ranged from ∼3.0 to ∼9.0 mag (see Figure 21). The five radio clumps are also located within the cluster, and only one of them (i.e. clump 'A'), which is estimated to be excited by an O9.5V star (see Table 2), is actually associated with at least three sources including the central bright source, as mentioned before. Estimation of the Lyman continuum flux for the remaining four radio clumps reveals that they are associated with sources earlier than B0.5V type, which are deeply embedded in the dense cloud without any NIR counterparts. This particular result indicates the formation of young massive stars in the cluster and that the region could be ionized by a small cluster of massive stars.

The bright source associated with the radio clump 'A' was characterized as a Herbig Ae/Be star by Deharveng et al. (1999), however, they suggested the presence of non-resolved binary (or multiple) system with the source, based on the radio spectral type and NIR data. We characterize this source as a Herbig Be star with the help of the multi-wavelength spectroscopic data (∼0.5–15 μm). The source is associated with the enhanced $H\alpha$ emission and has stellar mass ∼ 9M$_\odot$. The dynamical age of the radio clump 'A' is estimated to be about 0.16 to 0.54 Myr. In the field of massive star formation, it is often argued whether massive stars form before, after, or contemporary with the formation of low-mass stars (Tan et al. 2014). In this work, the average age of the low-mass stars appears to be higher than the ages of massive stars, indicating the formation of low-mass stars prior to the formation of massive stars. This result could be explained by the "outflow-regulated clump-fed massive star formation" model of Wang et al. (2010), where outflows fragment the filaments and choke the mass accretion rate such that massive stars gain masses gradually and form at the end of the cluster formation. High-resolution NH_3 line observations will be helpful to further investigate this theoretical explanation (Busquet et al. 2013).

Our multi-wavelength study is mainly concentrated towards the central 4.′6×4.′6 area in the Sh2-138 region. In order to examine the global star formation picture in the Sh2-138 region, we performed analysis of stellar content in the 15′×15′ area using YSOs identified from UKIDSS-GPS catalog. We generated 20NN density contours of YSOs following the method as discussed in Section 6.2. The 20NN surface density contours overlaid on the $Herschel$ 250 μm image are shown in Figure 22. Several prominent parsec-scale filamentary structures can be seen in the $Herschel$ 250 μm image (as mentioned in Section 4.1). The analysis of multi-wavelength data of the Sh2-138 region reveals that the cluster of YSOs harboring massive stars appears to be located at the junction of these filaments. Similar 'hub-filament' configuration has been reported in other cloud complexes, such as Taurus, Ophiuchus, and Rosette (e.g. Myers 2009; Schneider et al. 2012). In Rosette Molecular Cloud, Schneider et al. (2012) utilized the *Herschel* data along with the simulations of Dale & Bonnell (1990), and suggested that the infrared clusters were located at the junction of filaments or filament mergers. According to Myers (2009), a 'hub' region should have a typical peak column density of $\sim 10^{22}$ cm^{-2} which radiates several parsec-scale filaments associated with column densities of $\sim 10^{21}$ cm^{-2}. The filamentary structures identified in the Sh2-138 region appear to follow the similar conditions. The mean column density in the hub is $\sim 3 \times 10^{22}$ cm^{-2} and the hub is associated with the peak of 20NN contours of ∼50 YSOs pc^{-2} (also see Figure 17). Also, a cluster of YSOs is located with the highest density and the highest temperature region (see Figure 10). The high temperature of the central part suggests heating of gas from the energetics of massive stars located within the cluster. Formation of massive stars at the junction of filaments has also been found recently in the W40 region (Mallick et al. 2013) and IRAS 16148-5011 (Mallick et al. 2015). The multi-wavelength analysis of the central cluster (4.′6×4.′6) and the preliminary results in a larger area (15′×15′) suggest that an isolated cluster, which contains low and massive stars, is being formed at the 'hub' of filaments in the Sh2-138 region. In future, it will be useful to study the motion of the molecular material along the filaments to further investigate the role of filaments for the formation of YSO cluster.

8 CONCLUSIONS

We study the physical environment of the Sh2-138 region, a Galactic compact H II region, using multi-wavelength observations. We use new optical and NIR photometric and spectroscopic observations, as well as radio continuum observations, from Indian observational facilities. Additionally, we explore the region using archival public data covering radio through NIR wavelengths. This work provides a careful look at multi-wavelength data from 25 pc to 0.1 pc scale centered on IRAS 22308+5812. *Herschel* temperature and column density maps are utilized to examine the physical conditions in the region. Different line ratios are explored to estimate the physical properties of the central bright source. We study

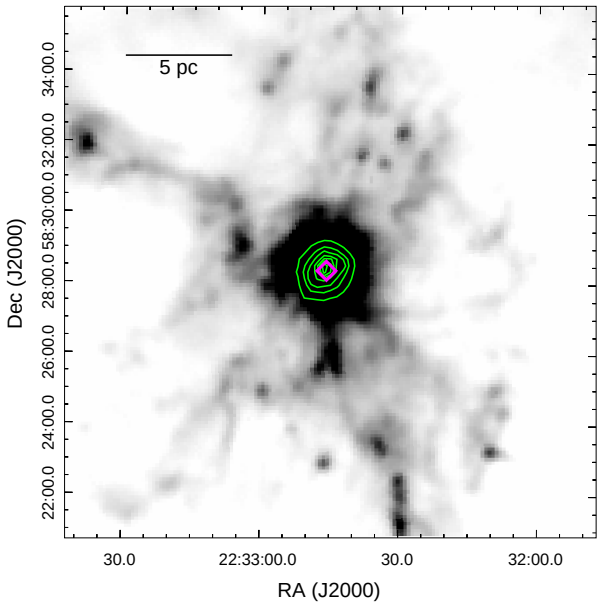

Figure 22. 20NN surface density contours of YSOs identified in $15' \times 15'$ region from UKIDSS catalog are overlaid on the $15' \times 15'$ *Herschel* 250 μm image. The position of the $IRAS$ source is marked by a diamond symbol ('$\diamondsuit$'). The contour levels are 5, 8, 11, 15, 18, 21, and 25 YSOs pc^{-2}.

the various CC-D and CM-D, and the surface density analysis, to investigate the embedded population in the region. The important conclusions of this work are as follows:

1. The analysis of optical (0.5-0.9 μm), NIR (1.0-2.4 μm), and MIR (5-15 μm) spectra of the central bright source, located near the $IRAS$ source, reveals that the source is a Herbig Be star. SED modeling of this source suggests that the source is young ($\sim$0.03 Myr) and has a mass of $\sim$9 M$_\odot$. In slitless spectra, two sources are identified with strong $H\alpha$ emission and one of them is the central bright source.

2. Using the NIR CC-D, NIR CM-D, and MIR CC-D as tool to distinguish the young stellar sources, we identified a total of 149 YSO candidates in the region and among these 149 young sources, 10 are Class I objects, 54 are Class II objects, and the remaining 85 are sources with infrared excess ($H - K > 0.9$) which could be candidate Class II/Class I YSOs. The $J/J - H$ CM-D analysis shows that the majority of YSOs have masses less than 4 M$_\odot$. Our K_s-band luminosity function fits to a slope of (α) 0.41$\pm$0.05, typical for young clusters.

3. Previously Deharveng et al. (1999) found four sources at the central part of the Sh2-138 cluster that are arranged in a similar configuration to that found in the Orion Trapezium cluster. We found that at least three of them are younger than 1 Myr and have spectral types earlier than B0, while two among them are $H\alpha$ emission stars.

4. A total of five clumps are identified in the high-resolution 1280 MHz radio continuum map and no optical/NIR counterparts are found for four of them. Assuming a single source is associated with each clump, we estimated the spectral types of all the sources to be earlier than B0.5. These results suggest the presence of embedded young massive stars in the Sh2-138 region. Free-free emission SED fitting of the central compact H II clump yields an electron density of 2250$\pm$400 cm^{-3}, while a lower electron density of 500$\pm$300 cm^{-3} is obtained from the [S II] 6716 to 6731 Å lines' ratio. The reason of this inconsistency is unknown. The dynamical age corresponding to the central clump, for an ambient density from 1000 to 10000 cm^{-3}, varies between 0.16 to 0.54 Myr.

5. Analysis of *Herschel* column density and temperature maps reveals that the region contains a large dust mass of $\sim$3770 M$_\odot$. The NN surface density analysis of YSOs reveals that the YSO cluster is located towards the highest column density ($\sim 3\times10^{22}$ cm^{-2}) and high temperature ($\sim$35 K) regime. The YSO cluster mainly contains low-mass stars as well as a few massive stars. The SED results and the CM-D analysis indicate that low-mass stars in the cluster are possibly formed prior to the formation of massive stars. The CO and dust condensation as well as radio continuum emissions are associated with the YSO cluster, where the signature of active star formation (i.e. outflow) is evident. Large scale morphology of the region suggests that the YSO cluster is being formed at the junction of *Herschel* filaments.

ACKNOWLEDGMENTS

We thank the anonymous referee for the useful comments and suggestions which helped to improve the scientific content of the paper. We thank the infrared group of TIFR for their support with TIRSPEC which is extensively used for observations of this region. We would like to thank the staff at IAO, Hanle and its remote control station at CREST, Hosakote for their help during the observation runs. We thank the staff at GMRT for their assistance during the observations. L.K.D. was supported by the grant CB-2010-01-155142-G3 from the CONACYT (Mexico) during this work. This publication uses data products from the Two Micron All Sky Survey, and the United Kingdom Infrared Telescope Infrared Deep Sky Survey. This work is based in part on observations made with the *Spitzer* Space Telescope, obtained from the NASA/IPAC Infrared Science Archive, both of which are operated by the Jet Propulsion Laboratory, California Institute of Technology under a contract with the National Aeronautics and Space Administration. This research uses the SIMBAD astronomical database service operated at CDS, Strasbourg. This publication made use data of 2MASS, which is a joint project of University of Massachusetts and the Infrared Processing and Analysis Centre/California Institute of Technology, funded by the National Aeronautics and Space Administration and the National Science Foundation.

REFERENCES

Aguirre J. E., et al., 2011, ApJS, 192, 4
Allamandola L. J., Hudgins D. M., Sandford S. A., 1999, ApJ, 511, L115
André P., et al., 2010, A&A, 518, L102
Battersby C., et al., 2011, A&A, 535, A128
Bessell M. S., Brett J. M., 1988, PASP, 100, 1134
Blitz L., Fich M., Stark A. A., 1982, ApJS, 49, 183
Bohlin R. C., Savage B. D., Drake J. F., 1978, ApJ, 224, 132
Buckle, J. V., Hills, R. E., Smith, H., et al. 2009, MNRAS, 399, 1026
Busquet G., et al., 2013, ApJ, 764, L26
Canto J., Meaburn J., Theokas A. C., Elliott K. H., 1980, MNRAS, 193, 911
Casali, M., Adamson, A., Alves de Oliveira, C., et al. 2007, A&A, 467, 777
Casertano S., Hut P., 1985, ApJ, 298, 80

Cohen J. G., Persson S. E., Elias J. H., Frogel J. A., 1981, ApJ, 249, 481
Condon J. J., Cotton W. D., Greisen E. W., Yin Q. F., Perley R. A., Taylor G. B., Broderick J. J., 1998, AJ, 115, 1693
Corcoran M., Ray T. P., 1998, A&A, 331, 147
Dale, J. E., & Bonnell, I. A. 2011, MNRAS, 414, 321
Deharveng L., Zavagno A., Nadeau D., Caplan J., Petit M., 1999, A&A, 344, 943
Di Francesco J., Johnstone D., Kirk H., MacKenzie T., Ledwosinska E., 2008, ApJS, 175, 277
Donehew B., Brittain S., 2011, AJ, 141, 46
Duchêne G., Kraus A., 2013, ARA&A, 51, 269
Felli M., Harten R. H., 1981, A&A, 100, 42
Fich M., 1993, ApJS, 86, 475
Finkenzeller U., 1985, A&A, 151, 340
Hamann F., Persson S. E., 1992, ApJS, 82, 285
Haslam C. G. T., Salter C. J., Stoffel H., Wilson W. E., 1982, A&AS, 47, 1
Hernández J., Calvet N., Hartmann L., Briceño C., Sicilia-Aguilar A., Berlind P., 2005, AJ, 129, 856
Hildebrand R. H., 1983, QJRAS, 24, 267
Hillenbrand L. A., Bauermeister A., White R. J., 2008, ASPC, 384, 200
Ho, P. T. P., Beck, S. C., Turner, J. L. 1990, ApJ, 349, 57
Holland W. S., et al., 1999, MNRAS, 303, 659
Indebetouw, R., Mathis, J. S., Babler, B. L., et al. 2005, ApJ, 619, 931
Johansson L. E. B., Olofsson H., Hjalmarson A., Gredel R., Black J. H., 1994, A&A, 291, 89
Jose J., et al., 2008, MNRAS, 384, 1675
Koenig X. P., Allen L. E., Gutermuth R. A., Hora J. L., Brunt C. M., Muzerolle J., 2008, ApJ, 688, 1142
Kurtz S., 2002, ASPC, 267, 81
Lada E. A., Depoy D. L., Evans N. J., II, Gatley I., 1991, ApJ, 371, 171
Lada C. J., Adams F. C., 1992, ApJ, 393, 278
Lada C. J., Alves J., Lada E. A., 1996, AJ, 111, 1964
Lada E. A., Lada C. J., 1995, AJ, 109, 1682
Landolt A. U., 1992, AJ, 104, 340
Launhardt R., et al., 2013, A&A, 551, A98
Lawrence A., Warren S. J., Almaini O., et al. 2007, MNRAS, 379, 1599
Lucas P. W., et al., 2008, MNRAS, 391, 136
Mallick K. K., Ojha D. K., Samal M. R., Pandey A. K., Bhatt B. C., Ghosh S. K., Dewangan L. K., Tamura M., 2012, ApJ, 759, 48
Mallick K. K., Kumar M. S. N., Ojha D. K., Bachiller R., Samal M. R., Pirogov L., 2013, ApJ, 779, 113
Mallick K. K., et al., 2014, MNRAS, 443, 3218
Mallick K. K., Ojha D. K., Tamura M., Linz H., Samal M. R., Ghosh S. K., 2015, MNRAS, 447, 2307
Martín-Hernández N. L., et al., 2002, A&A, 381, 606
Meyer M. R., Calvet N., Hillenbrand L. A., 1997, AJ, 114, 288
Mezger P. G., Henderson A. P., 1967, ApJ, 147, 471
Moran J. M., 1983, RMxAA, 7, 95
Myers P. C., 2009, ApJ, 700, 1609
Nielbock M., et al., 2012, A&A, 547, A11
Ninan J. P., et al., 2014, JAI, 3, 1450006
Ojha D. K., Ghosh S. K., Kulkarni V. K., Testi L., Verma R. P., Vig S., 2004a, A&A, 415, 1039
Ojha D. K., et al., 2004b, ApJ, 608, 797
Omar A., Chengalur J. N., Anish Roshi D., 2002, A&A, 395, 227
Osterbrock D. E., Ferland G. J., 2006, Astrophysics of gaseous nebulae and active galactic nuclei
Panagia N., 1973, AJ, 78, 929
Pilbratt G. L., et al., 2010, A&A, 518, L1
Qin S.-L., Wang J.-J., Zhao G., Miller M., Zhao J.-H., 2008, A&A, 484, 361
Reid M. A., Wilson C. D., 2006, ApJ, 644, 990
Reid M. A., Wilson C. D., 2005, ApJ, 625, 891
Robitaille T. P., Whitney B. A., Indebetouw R., Wood K., Denzmore P., 2006, ApJS, 167, 256
Robitaille T. P., Whitney B. A., Indebetouw R., Wood K., 2007, ApJS, 169, 328
Sadavoy S. I., et al., 2012, A&A, 540, A10
Schmeja S., 2011, AN, 332, 172
Schmeja S., Kumar M. S. N., Ferreira B., 2008, MNRAS, 389, 1209
Schneider N., et al., 2012, A&A, 540, L11
Sharma S., Pandey A. K., Ojha D. K., Chen W. P., Ghosh S. K., Bhatt B. C., Maheswar G., Sagar R., 2007, MNRAS, 380, 1141
Sharpless S., 1959, ApJS, 4, 257
Siess L., Dufour E., Forestini M., 2000, A&A, 358, 593
Simpson J. P., Rubin R. H., 1990, ApJ, 354, 165
Skrutskie M. F., Cutri R. M., Stiening R., et al. 2006, AJ, 131, 1163
Sloan G. C., et al., 2005, ApJ, 632, 956
Soderblom D. R., Hillenbrand L. A., Jeffries R. D., Mamajek E. E., Naylor T., 2014, prpl.conf, 219
Spitzer L., 1978, ppim.book,
Stahler S. W., Palla F., 2005, fost.book,
Stetson P. B., 1987, PASP, 99, 191
Strömgren B., 1939, ApJ, 89, 526
Swarup G., Ananthakrishnan S., Kapahi V. K., Rao A. P., Subrahmanya C. R., Kulkarni V. K., 1991, CuSc, 60, 95
Tan J. C., Beltrán M. T., Caselli P., Fontani F., Fuente A., Krumholz M. R., McKee C. F., Stolte A., 2014, prpl.conf, 149
Tej A., Ojha D. K., Ghosh S. K., Kulkarni V. K., Verma R. P., Vig S., Prabhu T. P., 2006, A&A, 452, 203
Vig S., Ghosh S. K., Ojha D. K., Verma R. P., Tamura M., 2014, MNRAS, 440, 3078
Wang P., Li Z.-Y., Abel T., Nakamura F., 2010, ApJ, 709, 27
Whitney B. A., Wood K., Bjorkman J. E., Cohen M., 2003a, ApJ, 598, 1079
Whitney B. A., Wood K., Bjorkman J. E., Wolff M. J., 2003b, ApJ, 591, 1049
Williams J. P., de Geus E. J., Blitz L., 1994, ApJ, 428, 693
Wouterloot J. G. A., Brand J., 1989, A&AS, 80, 149
Wright E. L., et al., 2010, AJ, 140, 1868
Zinnecker H., McCaughrean M. J., Wilking B. A., 1993, prpl.conf, 429
Zinnecker H., Yorke H. W., 2007, ARA&A, 45, 481